Project 068 Combustor Wall Cooling with Dirt Mitigation

The Pennsylvania State University

Project Lead Investigator

Reid A. Berdanier
Associate Professor
Department of Mechanical Engineering
The Pennsylvania State University
NARCO Building, CATO Park, Room 148
3127 Research Drive
State College, PA. 16801
(814) 863-3972
rberdanier@psu.edu

University Participants

The Pennsylvania State University (PSU)

- P.I.s: Prof. Karen Thole, Prof. Reid Berdanier, Dr. Michael Barringer, Prof. Stephen Lynch
- FAA Award Number: 13-C-AJFE-PSU-057
- Period of Performance: June 5, 2020, to September 30, 2025
- Tasks:
  1. Manufacturing and testing of combustor liner cooling concepts with small coupons
  2. Testing of scaled models of optimal cooling concepts
  3. Profile simulator for the Steady Thermal Aero Research Turbine (START)

Project Funding Level

For the entire 4-year effort ASCENT Project 068 received $1,250,000 Federal Aviation Administration (FAA) funding, and matching funds of $1,250,000 were provided by Pratt & Whitney.®

Investigation Team

Prof. Reid A. Berdanier (P.I.), Management, reporting, and oversight of all technical tasks
Prof. Karen A. Thole (co-P.I.), Management, reporting, and oversight of all technical tasks
Assoc. Prof. Stephen Lynch (co-P.I.), Management, reporting, and oversight of Tasks 1–3
Assoc. Res. Prof. Michael Barringer (research advisor), Task 3
Scott Fishbone (project manager), Tasks 1–3
Tom Houck (project manager), Tasks 1–3
Kyle McFerran (graduate student), Tasks 1 and 2
Chad Schaeffer (graduate student), Task 3

Project Overview

A critical issue related to the current operation of gas turbines is the ingestion of dirt and other fine particles that lead to dirt buildup and reduced cooling of hot section components, such as the liner walls of the combustion chamber. With increasing need to fly in dirty environments, the criticality of operations in dirty environments is increasing. Modern gas turbine engines typically use a double-walled combustor liner with impingement and effusion cooling technologies, whereby impingement cooling enhances the backside internal cooling, and effusion cooling creates a protective film of coolant along the external liner walls. Dirt accumulation on the internal and external surfaces severely diminishes the heat transfer capability of these cooling designs. This study also investigates the development of a combustor profile simulator upstream of the Steady Thermal Aero Research Turbine (START) test turbine. Combustor profiles affect turbine performance and durability. As combustor designs evolve, particularly the liner cooling technologies, understanding the impacts on the turbine is important. This study investigates practical designs applied to combustor walls to decrease dirt accumulation and also explores the development of a profile simulator that can replicate relevant temperature and pressure profiles upstream of a test turbine.

Task 2 – Testing of Scaled Models of Optimal Cooling Concepts

The Pennsylvania State University

Objective

The objective of this task is to produce an effective cooling design for combustor walls that is insensitive to dirt accumulation at existing or lower coolant flow rates. Various parameters such as dirt deposition, flow behavior, and heat transfer effectiveness will be investigated and quantified to compare the efficiency of candidate designs. Improved understanding of the underlying reasons for dirt sensitivity and deposition behavior is also being sought. During this past year, the ASCENT Project 068 team took two primary approaches to the problem: (1) identify the impact of dirt deposition on the cooling performance of a typical double-wall combustor liner and (2) identify a novel geometry to replace the double-wall liner design with a triple-wall combustor liner.

Research Approach

Background

The project focuses on the impacts of ingestion of dirt and other fine particulate matter in gas turbine engines. These particles are known to block the cooling holes and passages needed to effectively cool combustion chamber walls. Gas turbine engines often use double-walled combustor liners comprising impingement and effusion cooling plates (Figure 1). The impingement plate enhances backside internal cooling, and the effusion plate creates a protective film of coolant along the external liner walls. As particulate matter accumulates on these plates, the heat transfer performance severely decreases, thus ultimately leading to component failure.

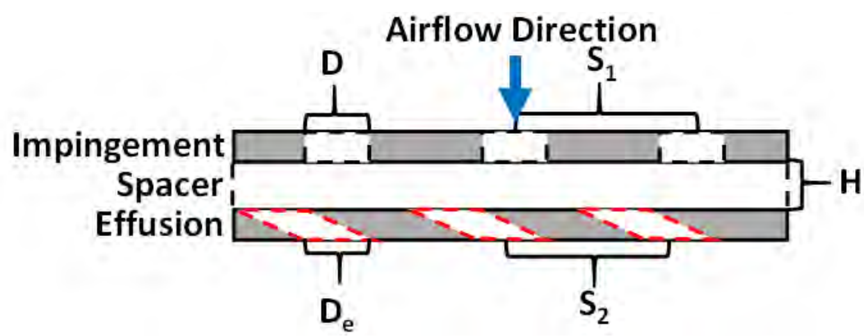

Figure 1. Schematic of double-walled combustor liner geometry.

A coupon design of a double-wall combustor liner consisting of an impingement, spacer, and effusion plate is shown in Figure 2, along with the testing facility in which the coupons are installed. The impingement plate has straight holes resulting in high-velocity jets that impinge on the backside of the effusion plate, which is exposed to the hot main gas path. The spacer plate creates a small controllable gap between the impingement and effusion plates. The effusion plate uses cooling holes angled at 30° to create a film effect along the external wall exposed to the hot combustion gases.

The goal of this research is to determine the impact of dirt deposition on the ability to cool the double wall containing the hot combustion gases in the gas turbine engine. To understand the effects of dirt deposition on the combustor cooling, heat transfer coefficients on all four surfaces (top and bottom of both the impingement and effusion plates) need to be calculated. A three-case proposal utilizing thermal resistive networks can be used to measure these respective heat transfer coefficients. Case 2, shown in Figure 3, demonstrates the resistive network for calculating the heat transfer coefficient on the bottom (cold) side of the effusion plate. This past year, work has been based on this specific case. A more in-depth description of the heat transfer experimental methodology is provided in last year's annual report.

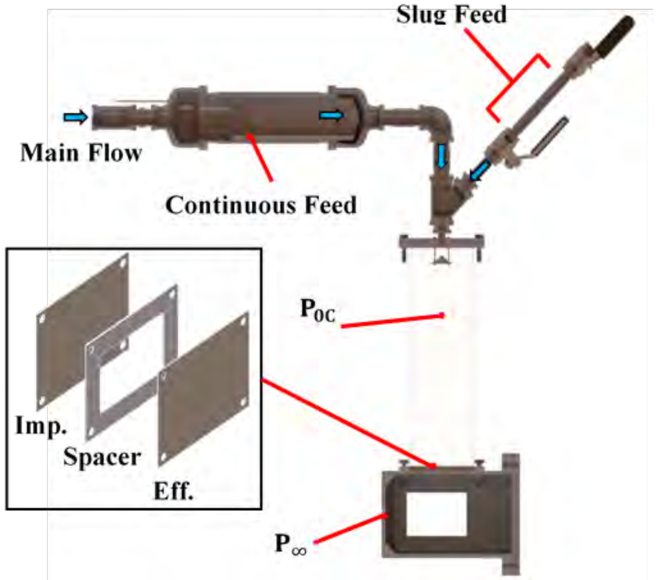

Figure 2. Schematic of the double-walled combustor liner configuration.

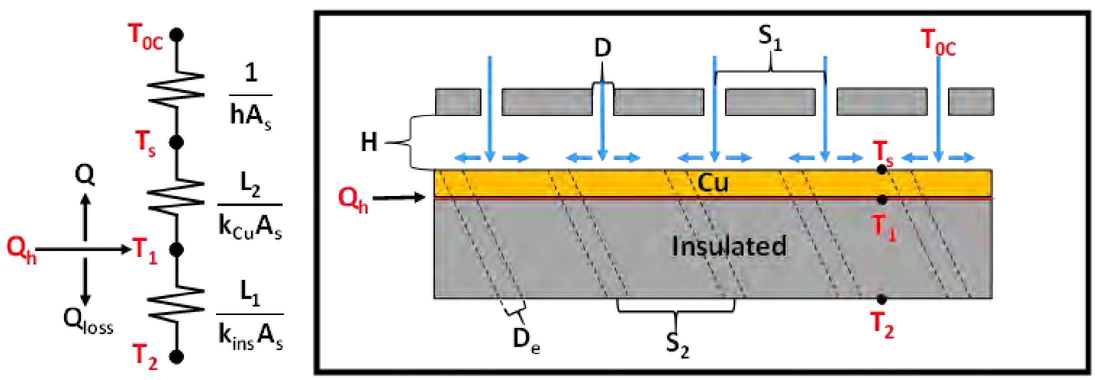

Figure 3. Thermal resistive network (left) used to calculate the convective heat transfer coefficient on the impinging side of an effusion plate. Next to the resistive network is the heater coupon (right) with dimensions used for heat transfer testing. Experimentally measured values are shown in red.

The three cases allow for calculation of the four heat transfer coefficients for dirt and no-dirt tests. In each case, one of the cooling plates is made of insulation, whereas the other plate is made of copper, an electric heater, and insulation. For the resistive network in Figure 3, the composite coupon made up the effusion plate. Of note, testing last year was performed with an effusion plate without effusion holes. Effusion holes were not evaluated because literature data were available for only plates without effusion holes. Five thermocouples were implemented throughout the composite coupon to measure the appropriate temperatures in the thermal resistive network. Ultimately, these thermocouple measurements were used to solve the heat transfer coefficient (h_1) in Equation 1.

$$h_1 = \frac{Q}{A_s(T_s - T_{0C})} \quad \text{(Eq. 1)}$$

Impacts of Dirt Deposition on a Double-Wall Liner Design

Heat transfer tests are performed using the dirt test rig shown in Figure 2. Last year, convective heat transfer results were shown for a no-effusion heater coupon for several height to diameter (H/D) ratios, where this ratio was adjusted by changing the spacing between the impingement and effusion plates. This year, heat transfer tests were performed on an effusion plate with effusion holes, shown in Figure 4, over a range of H/D values between 3 < H/D < 10. An array of 5 x 11 cooling holes was used for both the impingement and effusion plates, with effusion holes being angled at 30° with respect to the horizontal surface.

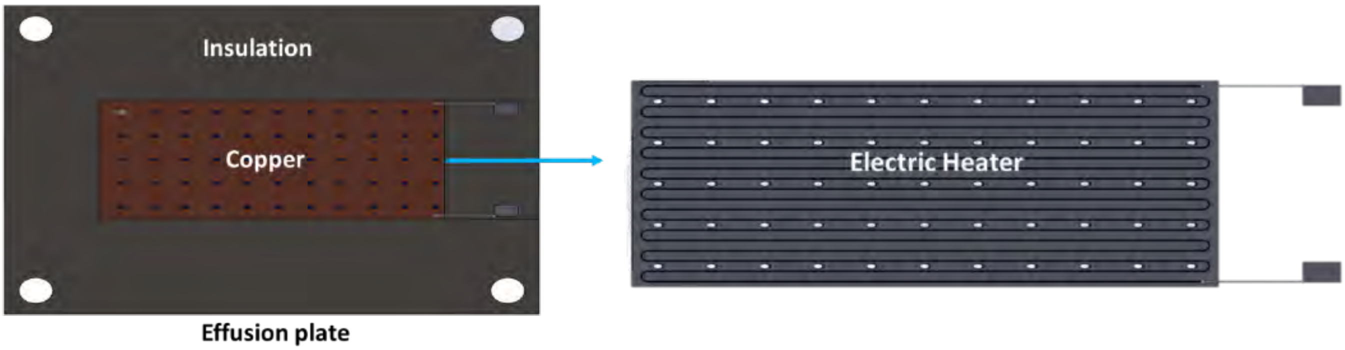

Figure 4. Heater composite consisting of insulation, an electric heater, and copper used for heat transfer testing of the effusion hole test plate.

Two different injection amounts were evaluated in this study, which led to two different testing conditions: (1) matched deposition and (2) matched supply. For the matched deposition condition, a mass of dirt was injected that resulted in 0.175 ± 0.015 g of dirt accumulation on the test plate surface. A target deposition mass of 0.175 g was chosen because prior dirt tests in the lab had similar deposition masses. The mass of injected dirt needed to achieve this matched deposition varied between 2 to 4.8 g for different mass flow rates and plate-to-plate spacings. In contrast, a constant 2 g of dirt was injected for the matched supply tests, which resulted in deposition masses between 0.05 to 0.175 g on the test plate surface. Overall, the two test conditions were conducted to isolate the effects of deposition mass and injection mass on the heat transfer coefficients (HTC).

For the heat transfer testing of the effusion plate without cooling holes, a constant Reynolds number (Re_d) was maintained throughout the dirt injection process. In contrast, a constant pressure ratio (PR) was maintained during dirt injection for the heat transfer testing on the effusion-cooled plate. Pressure taps located upstream of the impingement plate and downstream of the effusion plate were used to monitor the PR across the double-walled liner with Equation 1. A PR range of 1.01 < PR < 1.1 was evaluated for the effusion-cooled plate.

$$\mathrm{PR} = \frac{P_{0C}}{P_{\infty}} \qquad \text{(Eq. 2)}$$

As dirt was injected into the system, the upstream mass flow rate (and hence pressure) decreased, because dirt blocked the impingement and effusion cooling holes, thus reducing the overall flow area. The flow parameter (FP), shown in Equation 3, was monitored during testing to quantify these blockage levels caused by the deposition.

$$\mathrm{FP} = \frac{4\dot{m}\sqrt{RT_{0C}}}{\pi P_{0C} N D_i^2} \qquad \text{(Eq. 3)}$$

With the FP being directly related to the mass flow rate, a decrease in the mass flow rate resulting from the blockage of cooling holes leads to a reduction in FP (RFP). An increase in flow blockage is quantified by an increase in the RFP, which is defined in Equation 4.

$$\mathrm{RFP} = \frac{\mathrm{FP_{clean}} - \mathrm{FP_{dirty}}}{\mathrm{FP_{clean}}} \times 100 \qquad \text{(Eq. 4)}$$

Heat transfer coefficients for the dirty plate were less than those for the clean plate for all tests conducted in this study. The addition of dirt on the test plate surface had a twofold effect on the heat transfer. First, the deposition functioned as an extra layer of insulation which shielded the test plate from the cooling air. Second, the deposition structures that formed impacted the flow field of the impinging jets, which also led to reductions in cooling. Augmentations that compared Nusselt numbers (Nu) for the dirty (Nu_d) and clean (Nu_0) test plates, as defined in Equation 5, gave insight into the negative effects the deposition had on cooling within the double-walled liners. The augmentation is a positive number because the addition of dirt always led to reductions in the HTC (and hence Nusselt number). This reduction in the HTC is representative of a cooling reduction on the target plate surface. As the reductions in cooling from dirt accumulation increased, the augmentation increased.

$$\text{Augmentation} = \frac{Nu_0 - Nu_d}{Nu_0} * 100 = \left.\frac{\Delta Nu}{Nu_0}\right|_{Re_d, PR} \quad \text{(Eq. 5)}$$

The augmentations compare reductions in Nusselt numbers at a constant Red or at a constant PR. The results of this current study are the basis of a new literature paper that was written and submitted to the 2024 Turbo Expo Conference (McFerran et al., 2025). For the effusion hole plate, this means that the dirty HTC was compared to the clean HTC at the dirty Re_d for the Re_d-based augmentation and at the clean Re_d for the PR-based augmentation. In Figure 5, an example Re_d- and PR-based augmentation for the effusion hole plate is shown for a PR = 1.045. There is a reduction in the flow for the same pressure ratio due to blockage where Re_d decreased from Re_d = 1800 (clean) to 1200 (dirty). The augmentation then compares the dirty Nu at Re_d = 1200 to the clean Nu predicted by the clean trendline at Re_d = 1200 and 1800 for the Re_d- and PR-based augmentation, respectively. Testing performed on the no-effusion plate maintained a constant Re_d so only Re_d-based augmentations could be made between the dirty and clean HTCs which is also shown in Figure 5.

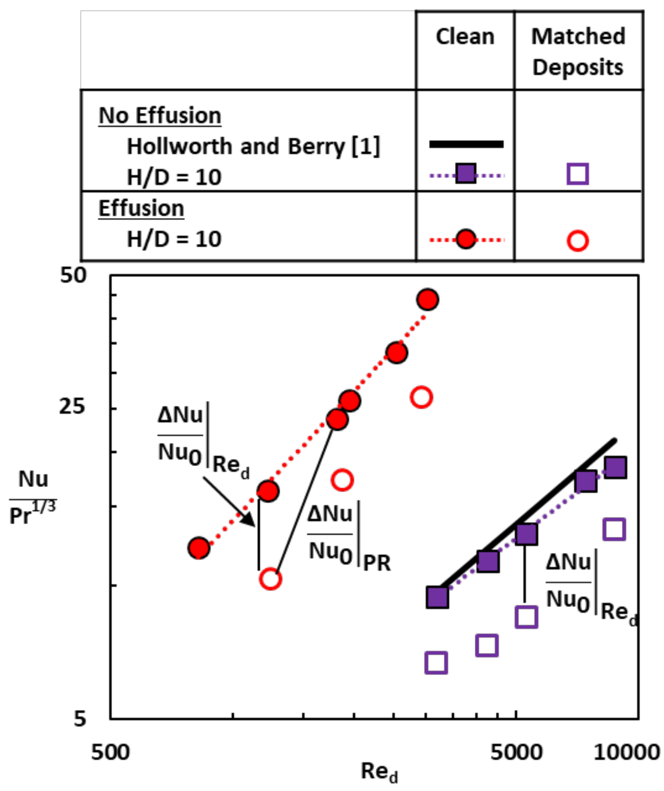

Figure 5. Heat transfer coefficient in terms of a Nusselt number as a function of Red for both test plates at a H/D = 10. Dirty heat transfer measurements have 0.175 g of deposition on the cold-side effusion plate surface. Example augmentations are shown for each test plate.

Heat transfer results in terms of a Nusselt number are plotted in Figure 6 as a function of Reynolds number (Re_d) for the effusion hole plate over a range of H/D from 3 < H/D < 10 and Re_d from 800 < Re_d < 3500. This Re_d range corresponds to the range of pressure ratios evaluated which were between 1.01 < PR < 1.1. Heat transfer coefficients for the clean and dirty plates are shown in Figure 6, where dirty tests had 0.175 g of dirt deposition on the effusion plate surface. The heat transfer results for the no effusion plate are also shown for 10 < H/D < 15 for a Re_d range of 3200 < H/D < 8400. The range of Re_d for the no-effusion plate was chosen to match the literature, and it differed from the Re_d range for the effusion hole plate because the effusion hole plate was designed to match typical combustor liner pressure ratios. Heat transfer coefficients for the effusion hole plate are 300% higher than those for the no-effusion plate. A higher heat transfer coefficient indicates better cooling, which would be expected for the effusion hole plate because of the cooling that occurs through the coupon from the effusion holes. These results verified that having effusion holes led to enhanced cooling on the cold-side effusion plate surface. The addition of effusion holes led to improved internal cooling of the effusion plate. Additionally, less crossflow resulted on the cold-side surface of the effusion hole plate compared to the no-effusion plate because air exited through the effusion holes and not out of the sides. Increasing the crossflow reduced the strength of the impinging jets which diminished the cooling for the no-effusion plate.

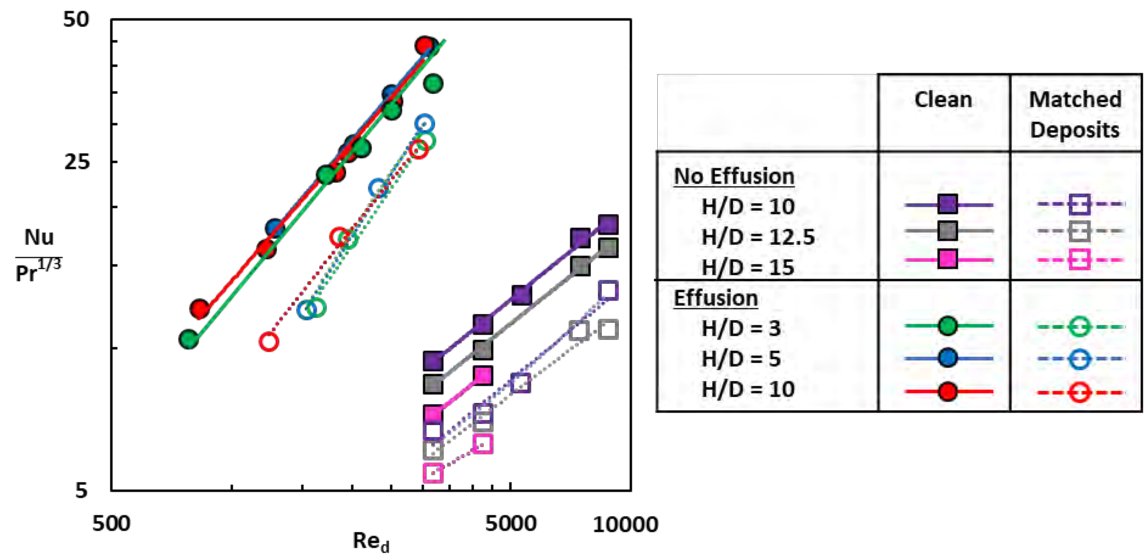

Figure 6. Heat transfer results in terms of a Nusselt number as a function of Reynolds number for both the effusion plate without cooling holes and the effusion-cooled plate.

For all tests performed on the no-effusion plate, an increase in the plate-to-plate spacing resulted in lower HTCs, which means less cooling. In contrast, the effusion hole plate showed no differences in HTCs for an increase in plate to plate spacing. These results can be explained by the localized flowfield effects of heat transfer that resulted from the jet flow (Gardon & Arkfirit, 1966; Gardon & Arkfirit, 1965; Choi & Kim, 2022). As the impinging jet traveled towards the target surface, a momentum exchange with the surrounding fluid leads to development of a shear layer that expands as the plate-to-plate spacing increases. This shear layer leads to a decrease in the centerline jet velocity. As the plate-to-plate spacing increases, the diminishing centerline velocity combined with a widening of the jet leads to a decreasing HTC at the stagnation point (Gardon & Arkfirit, 1966; Choi & Kim, 2022). As shown in the literature for up to H/D of 8, there is an increase in the mixing of the jet with the surrounding fluid from increased turbulence, which leads to increased heat transfer in the jet stagnation region (Gardon & Arkfirit, 1966; Choi & Kim, 2022). This increase in heat transfer from turbulence dominates the decrease in heat transfer from diminishing centerline velocities and widening of the impinging jets as H/D increases to 8. Gardon and Akfirat (1965) showed that beyond H/D of 8, the turbulence intensity (TI) did not continue to increase and that the decreasing jet velocity and increasing jet width began to dominate, decreasing the stagnation HTC. The data shown in Figure 6 support their finding on why HTCs for the no-effusion plate decreased as H/D increased beyond 10.

Another important finding by previous studies (Gardon & Arkfirit, 1966; Choi & Kim, 2022) is that heat transfer performance at H/D less than 10 was affected by the formation of a secondary peak in heat transfer radially out from the stagnation region due to the boundary layer transitioning from laminar to turbulence. As H/D decreased from 10, which encompasses the 3 < H/D < 10 range evaluated for the effusion hole plate, these secondary spikes in heat transfer resulted in increased HTCs radially out from the stagnation region. These physics explain the average HTC trends for an increasing H/D from 3 to 10, where the increase in stagnation zone heat transfer and decrease in lateral downstream heat transfer led to equivalent average heat transfer coefficients for the changing H/D on the effusion hole plate.
A computational study performed by Choi and Kim (2022) also showed that average HTCs were constant over a H/D range of 1-10 for an effusion hole plate.

The accumulation of dirt on both test plates led to a reduction in the HTC for all plate-to-plate spacings as shown in Figure 6. Re_d- and PR-based augmentation results for both test plates are shown in Figure 7 over several Re_d and PRs. It is important to note the magnitude of these augmentations range between 20-55%, which signifies the highly negative impact dirt has on cooling performance in a double-walled liner. As a reminder, a higher augmentation represents a higher reduction in the HTC and hence a higher cooling reduction due to dirt. In Figure 7, the effusion hole plate with a matched supply had an increase in Re_d-based augmentations as the plate-to-plate spacing increased, which shows that the reductions in the HTC from dirt increased as H/D increased.

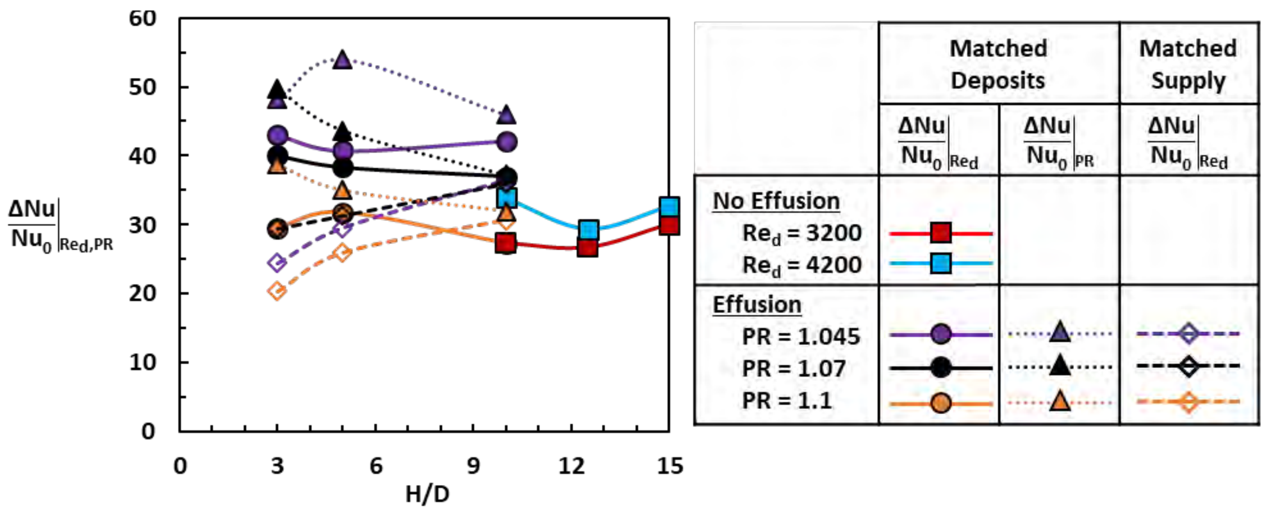

Figure 7. Re_d- and PR-based augmentations comparing the heat transfer coefficient for the clean and dirty plates across a range of H/D for both test plates. For matched deposits, 0.175 g of dirt was on the test plate surface; for matched supply, a total of 2 g of dirt was injected.

For matched deposit cases, both test plates demonstrated a constant Re_d-based augmentation as a function of the H/D ratio. In contrast, PR-based augmentations for matched deposits on the effusion hole plate show that an increase in H/D led to a decrease in cooling reductions. Overall, the PR augmentations, which are more representative of true engine conditions, are higher than all of the Re_d augmentations for a constant H/D. As H/D increased, the difference between the PR- and Re_d-based augmentations decreased. This result has to do with the RFP, which is shown to decrease as H/D increased for the effusion hole plate in Figure 8. As the RFP decreased, the difference between the clean and dirty Re_d also decreased, which would lead to decreased differences between the PR and Re_d-based augmentations.

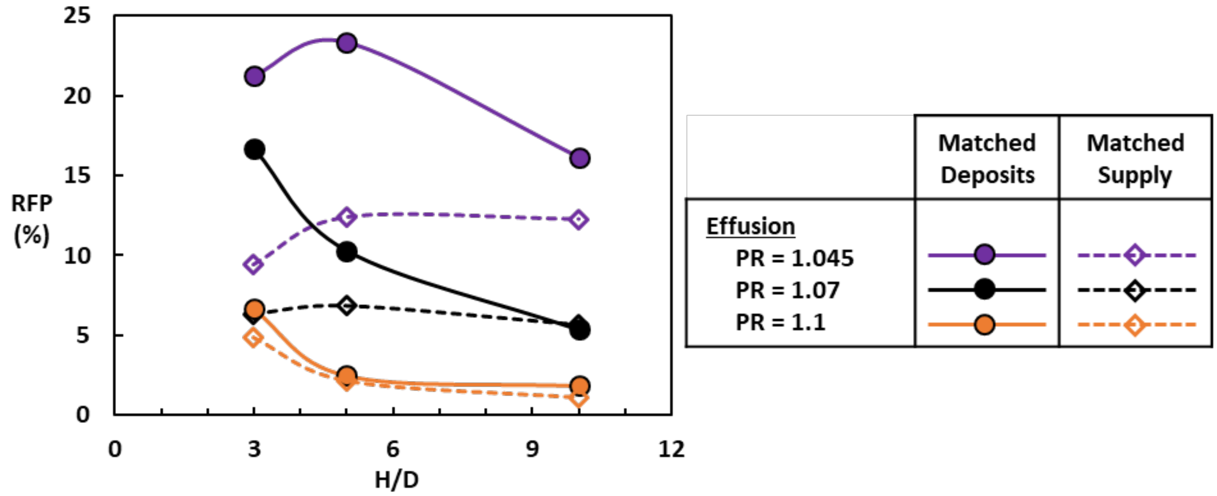

Figure 8. RFP as a function of H/D for the effusion hole plate. For matched deposits, 0.175 g of dirt was on the test plate surface; for matched supply, a total of 2 g of dirt was injected.

For a matched deposition, there was at least a 3% reduction in the RFP as the plate-to-plate spacing increased from 3D to 10D, as shown in Figure 8. The PR-based augmentations in Figure 7 for the effusion hole plate followed similar trends to the RFP trends in Figure 8 for a matched deposit. For a matched supply, the RFP was constant as a function of H/D as shown in Figure 8. Although not plotted, the PR-based augmentation followed a similar trend to this RFP, which demonstrates that RFP is an important predictor of the PR-based augmentations.

Different dirt injection amounts explain the RFP trends observed as a function of H/D. Throughout the testing, the amount of dirt needed to achieve matched deposition amounts decreased as H/D increased, which suggests that dirt was more readily captured on the effusion hole plate surface as the plate-to-plate spacing increased. For example, at a PR of 1.045, the injected mass of dirt needed to reach matched deposits on the effusion hole plate for a H/D of 10 was 2.8 g, but for a H/D of 3, an injection mass of 4.4 g was needed. An explanation for this trend resides in experimental observations made on the back-side impingement plate surface, which showed a decrease in dirt buildup as H/D increased. These observations suggest that as H/D increased, the dirt was less likely to rebound off of the effusion plate surface and stick to the impingement plate, leading to more deposition on the test plate surface.

With the injection mass decreasing for matched deposits as H/D increased, it is no surprise that the RFP also decreased in Figure 8. From the standpoint of flow blockage, it would be expected that a decrease in RFP would correlate with a decrease in the Re_d-based augmentation. However, Figure 7 showed that the Re_d-based augmentation was constant as a function of H/D for a matched deposit, which contradicts the RFP trends.

Likewise, for the matched supply case, the RFP was constant as a function of H/D as shown in Figure 8, which suggests that plate-to-plate spacing had minimal impact on the RFP. However, the Re_d-based augmentation shown in Figure 7 increased as H/D increased. These results suggest that the deposition structures must be considered to fully understand the cooling reductions.

The deposition patterns for different H/Ds are shown in Figure 9 for both test plates with a matched deposit. For the no-effusion plate, as the plate-to-plate distance increased from 10D to 15D, the conical mound region became flatter with decreasing peak heights. These results align with the flow field physics of the jet widening as the H/D increased which led to wider, flatter deposition structures (Fallon et al., 2023).

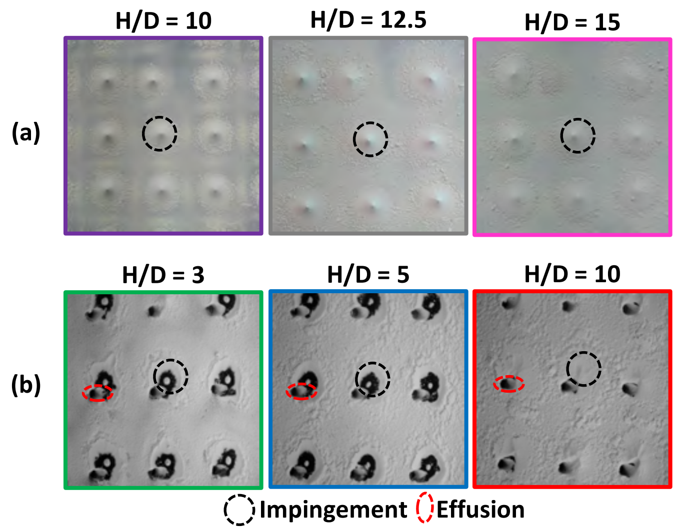

Figure 9. Observed deposition patterns across a H/D range of 3 < H/D < 15 for (a) the no-effusion plate at a Red = 3200 and (b) the effusion hole plate at a PR = 1.045. A black dotted circle is the impingement location, and a red dotted circle is the effusion hole.

For the effusion hole plate, an increase in the plate-to-plate spacing showed an increase in stagnation region deposition. The centerline velocity decreased as H/D increased and, as a result, the decreased velocity led to more deposition in the stagnation region which is clearly shown in Figure 9b. Additionally, a H/D of 3 and 5 for the effusion hole plate showed development of a conical mound in the center of a black ring, which was the exposed test plate. Surrounding this region are dirt thicknesses that have a crater-like topology, which align with the boundary layer regions that transition from laminar to turbulent flow.

Three-dimensional scanning of the test plates provided a quantitative analysis of deposition thicknesses for both test plates over a range of plate-to-plate spacings. In Figure 10, laterally averaged dirt thicknesses for the effusion hole plate at a PR = 1.045 with matched deposition show the trends discussed previously for the observed deposition, specifically those regarding the stagnation region peak heights. It is important to note that the lateral average plots are not the actual deposition heights but rather a line average. For example, the stagnation region peak averaged with an area of no dirt buildup will result in a peak that is half of the stagnation peak height.

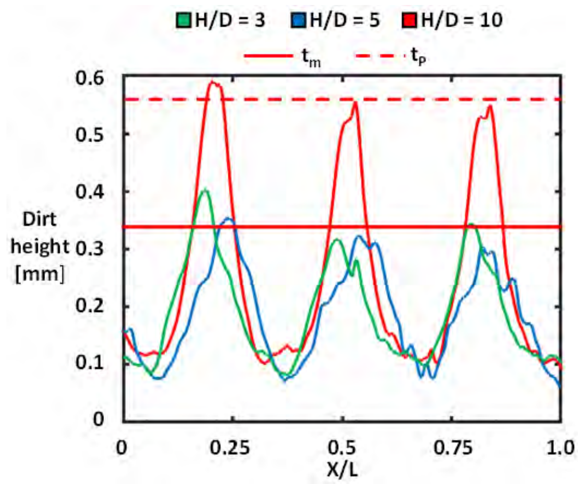

Figure 10. Laterally averaged dirt heights for the effusion hole plate at a PR of 1.045 for 3 < H/D < 15. The mean dirt thickness (tm) and the peak dirt thickness (tb) are shown for the effusion hole plate at H/D = 10.

For the no-effusion plate, it was observed that as H/D increased, the peak height decreased, which was a result of the jet width increasing. In contrast, the peak height increased as H/D was increased from 3 to 10 for the effusion hole plate, which is shown in Figure 10. This difference was a result of the decreasing centerline velocity that occurred over this H/D range. Cooling reductions, shown in Figure 7, were more severe for the effusion hole plate with a matched supply as H/D increased, which correlated well with the peak height increasing. The stagnation zone where the conical mounds formed is the region of dominant heat transfer, so if more dirt accumulated in this region, increased augmentations (and hence increased cooling reductions from dirt) would be expected. This result explains why the Re_d-based augmentation (Figure 7) is constant for the matched deposition test as a function of H/D. For an increase in H/D, the beneficial results of a decreasing RFP are countered by the increased deposition in the jet stagnation region. These results demonstrate that in addition to the level of flow blockage, the deposition structures play an important role in the reductions of heat transfer.

Mean (t_m) and peak (t_p) thicknesses were calculated from the lateral averages, as shown for the effusion hole plate at a H/D of 10 in Figure 10. These values were used to calculate an effective heat transfer coefficient that incorporated a uniform layer of dirt having these heights onto the cold-side effusion plate surface, where usage of t_p resulted in the most extreme approximation. This extra layer of dirt adds an insulating effect in the thermal resistive network from Figure 3. Even with this extra conductive layer of thickness, the convection accounted for at least 76%-92% of the total thermal resistance between the heater surface and the impinging free stream across all tests using the peak height thickness, t_p. This quantitative analysis supports the conjecture that the influence of the deposition topology on the impingement flow field is an important factor in the observed reductions on cooling.

Next, the effects of jet Reynolds number on heat transfer rates were analyzed. The convective heat transfer is highly dependent on the impinging Re_d. Referring back to Figure 6**,** the HTC increased as the Re_d increased for both test plates. Dirt deposition led to cooling reductions, which are shown in terms of a Re_d-based augmentation as a function of Re_d in Figure 11 for both test plates. Augmentation results are presented as a function of Re_d so that comparisons could be made for both test plates. For the no-effusion plate, Re_d-based augmentation results in Figure 11 show that the cooling reductions from dirt have a local maximum as a function of Re_d for a H/D of 10. At this H/D of 10, there is a local maximum of 35% in the augmentation at a Re_d = 5300.

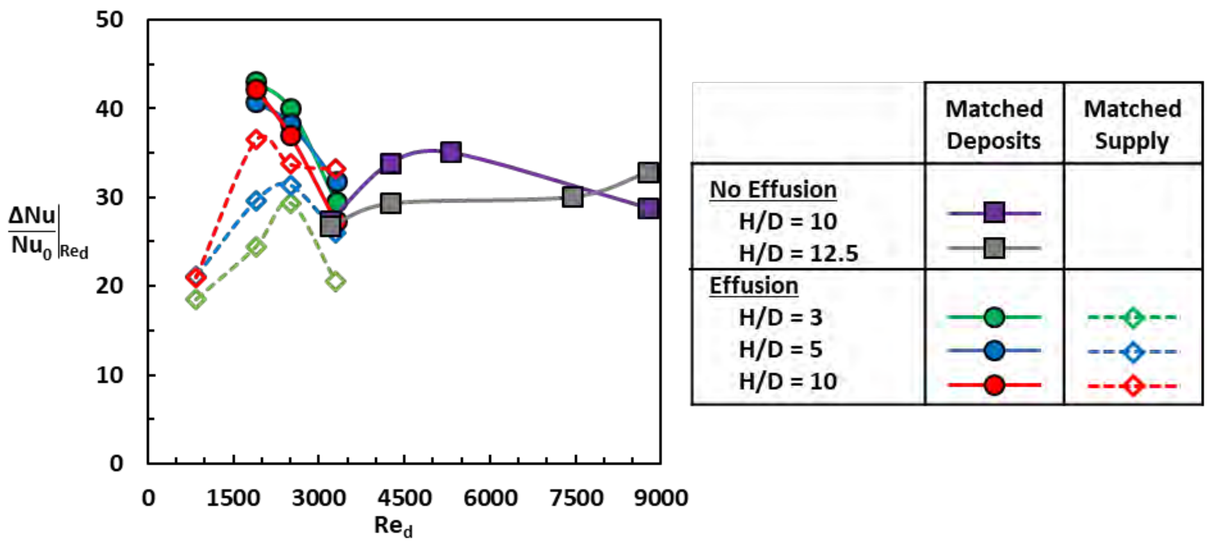

Figure 11. Re_d-based augmentation comparing the heat transfer coefficient for the clean and dirty plates across a range of Re_d for both test plates. For matched deposits, 0.175 g of dirt was on the test plate surface; for matched supply, a total of 2 g of dirt was injected.

Similarly, the effusion hole plate appeared to follow a similar trend, at least for a matched dirt supply condition. Over a Re_d range of $850 < Re_d < 3300$, which corresponded with the range of PR from $1.02 < PR < 1.1$, the effusion hole plate had a maximum in augmentation at a Re_d between 1800-2500 for all H/D. These augmentation results show that for a given H/D, there was a Re_d that had the most negative effects on cooling.

For a matched deposit condition, data were only obtained for a PR between 1.045-1.1 because the amount of dirt needed to achieve 0.175 g of dirt deposition was unfeasible due to the high RFP. However, for the range of PR evaluated, there was a strong trend showing that as the Re_d increased (and PR increased), the reductions in cooling decreased. PR-based augmentation results are not shown in Figure 11, but followed similar trends as the RFP which are shown in Figure 12.

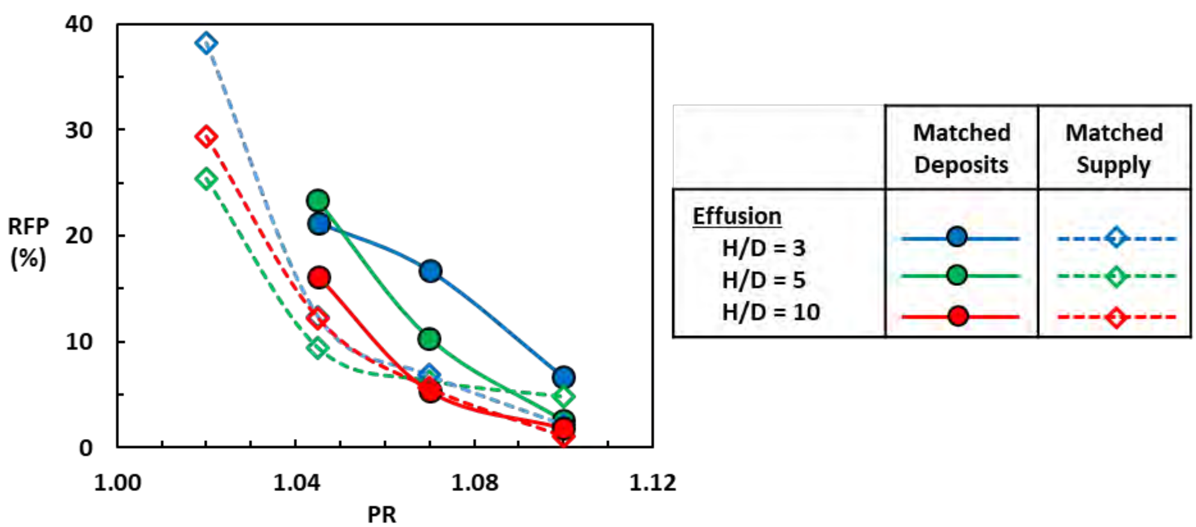

Figure 12. RFP as a function of PR for the effusion hole plate for 3 < H/D < 10. For matched deposits, 0.175 g of dirt was on the test plate surface; for matched supply, a total of 2 g of dirt was injected.

The RFP in Figure 12 shows a strong correlation between increasing PR and decreasing RFP for the effusion hole plate, which shows that as the jet velocity increased, the blockage of the cooling holes also decreased. This result occurred because an increasing flow velocity pushed more dirt through the impingement and effusion holes. Overall, with less blockage occurring as the pressure ratio increased, it is reasonable that the reductions in cooling also decreased because more of the impinging flow could impact the effusion plate surface and properly exit through the cooling holes.

The only exception to this trend occurred as the PR decreased from 1.045 to 1.02 for a matched supply, where an increase in the RFP did not correlate with an increase in the cooling reductions shown in Figure 12. This trend is observed because as the PR was decreased, the amount of dirt buildup on the effusion plate surface decreased, which overcame the effects of an increasing RFP. For example, a PR of 1.02 at a H/D of 3 yielded 0.058 g of deposition on the effusion plate, while a PR of 1.1 yielded a mass of 0.130 g. As the deposition mass decreased, the heat transfer augmentations also decreased because the effects the deposition had on the flow field were less severe. For a given H/D, it is believed that there is a Red value at which these effects of decreasing plate deposition mass begin to dominate the effects of RFP. This is another example demonstrating that flow blockage and the deposition structures both play equally important roles in cooling reductions.

Matched deposit dirt structures are shown for both test plates over several mass flow rates in Figure 13. For both test plates, there was a decrease in the peak height and greater overall spread of dirt as the mass flow increased. For the matched deposit case on the effusion hole plate, the decreasing RFP and decreasing peak heights aligned with a decreasing cooling reduction as the Red increased. As was stated previously, a decreasing deposition thickness in the jet stagnation region led to less severe effects on the HTC because this was the dominant area of heat transfer.

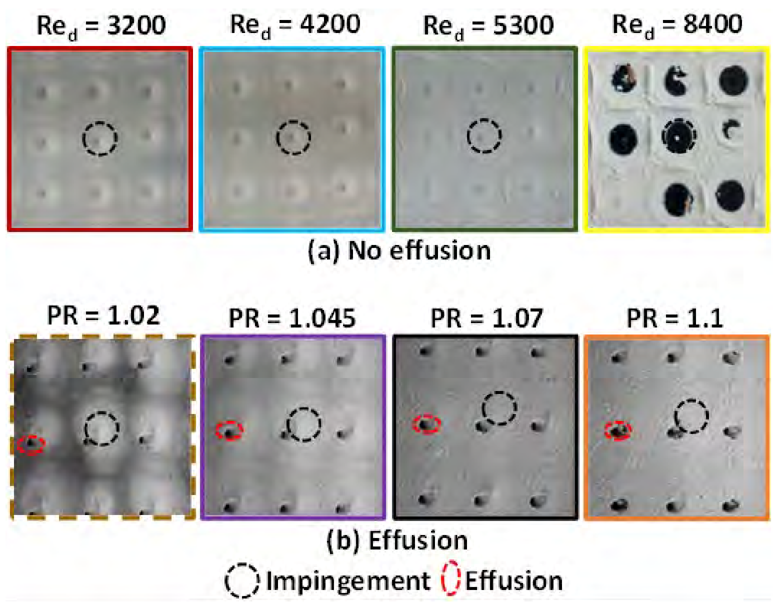

Figure 13. Observed deposition patterns for (a) the no-effusion plate and (b) the effusion hole plate for several mass flow rates at a H/D = 10. All deposition patterns are for a matched deposit, except for the effusion hole plate at a PR = 1.02 which is shown for a matched supply. A black dotted circle denotes the impingement jets, and a red dotted circle denotes the effusion holes.

Also shown in Figure 13 are deposition patterns for a PR of 1.02 with a matched supply. Outside of deposition in the stagnation region, there was little spread of dirt across the test plate surface as indicated by the black regions on the surface. This observation supports the decreased augmentation from PR of 1.045 to 1.02 because an increased area on the effusion plate surface was directly exposed to the cooling flow, which led to decreased cooling reductions. A similar observation for the no-effusion plate explains why the augmentation in Figure 11 is less for a Re_d of 3200 than that for Re_d of 5300, which had a greater spread of dirt.

Scans of each of the deposition patterns in Figure 14 were used to show side-view lateral averages of the deposition thicknesses for the effusion hole plate at a H/D of 10. Laterally averaged results are only shown for the effusion hole plate because both plates showed similar trends for a changing mass flow rate. The laterally averaged results show the decreased peak heights as the flow rate was increased. It is also interesting to see how the ridge region thickness at an X/L of 0.35 and 0.65 increased as the PR increased, which shows the dirt was pushed away from the jet stagnation zone.

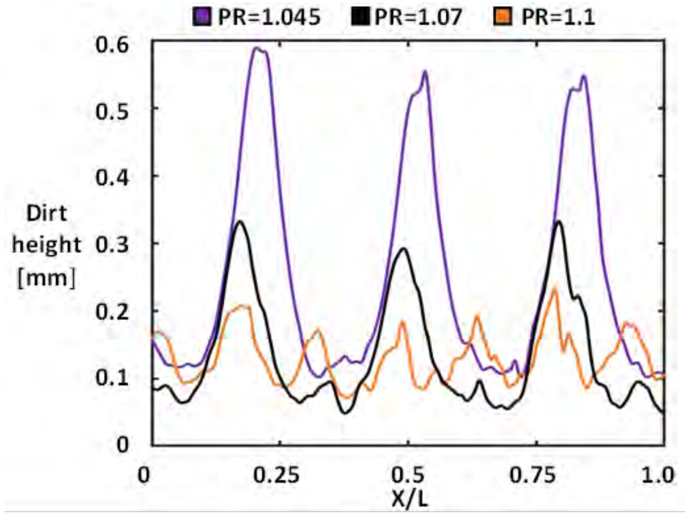

Figure 14. Laterally averaged dirt heights for the effusion hole plate for 1.045 < PR < 1.1 at a H/D of 10.

In summary, heat transfer testing was performed on an effusion hole plate holes for several pressure ratios and H/Ds. Overall, heat transfer coefficients are higher for the effusion hole plate compared to the coefficients obtained in prior quarters on a no-effusion plate. The effects of plate-to-plate spacing on cooling differed for the two test plates. For the clean, no-effusion plate, increasing the H/D from 10 to 15 resulted in a decrease in heat transfer. In contrast, for the clean, effusion hole plate, an increase in H/D from 3 to 10 resulted in similar heat transfer coefficients. The impingement flow physics explains why these heat transfer results occurred. An analysis of the flow blockage, deposition thickness, and deposition mass showed that decreasing all three were important factors in less severe cooling reductions.

Changing the jet Reynolds number and pressure ratio also impacted how deposition influenced target plate heat transfer. As the PR increased, the level of flow blockage in the impingement and effusion holes decreased, which suggested that greater flow rates resulted in more dirt being pushed through the cooling holes. Likewise, increased Red led to decreased dirt deposition heights and hence to decreased cooling reductions. It was observed that a decrease in the deposition mass, deposition height, and RFP all affected the heat transfer coefficients.

Novel Triple-Wall Combustor Liner

In developing methods for a dirt-insensitive combustor liner, a triple-walled liner was designed to include an additional impingement plate upstream of a double-walled liner, as seen in Figure 15b. The middle impingement plate, Imp-025, and the effusion plate, Eff-033, were designed in a similar fashion to prior double walled liners from our lab, which consisted of 5 x 11 arrays of cooling holes (Fallon et al., 2023). The three-digit number following each of the plate names represents the diameter of the cooling holes, where 025, for example, means 0.025 inches. Impingement holes were perpendicular to the effusion plate surface and offset from the effusion hole entrances, which were angled at 30° with respect to the horizontal surface. The Imp-025 and Eff-033 plates were used for all baseline 2-layer testing performed during this quarter, as seen in Figure 15a. An impingement plate, Imp-06, with cooling holes in a 4 x 10 array was added upstream of this double-walled liner for the purpose of encouraging more dirt capture on Imp-025 than Eff-033.

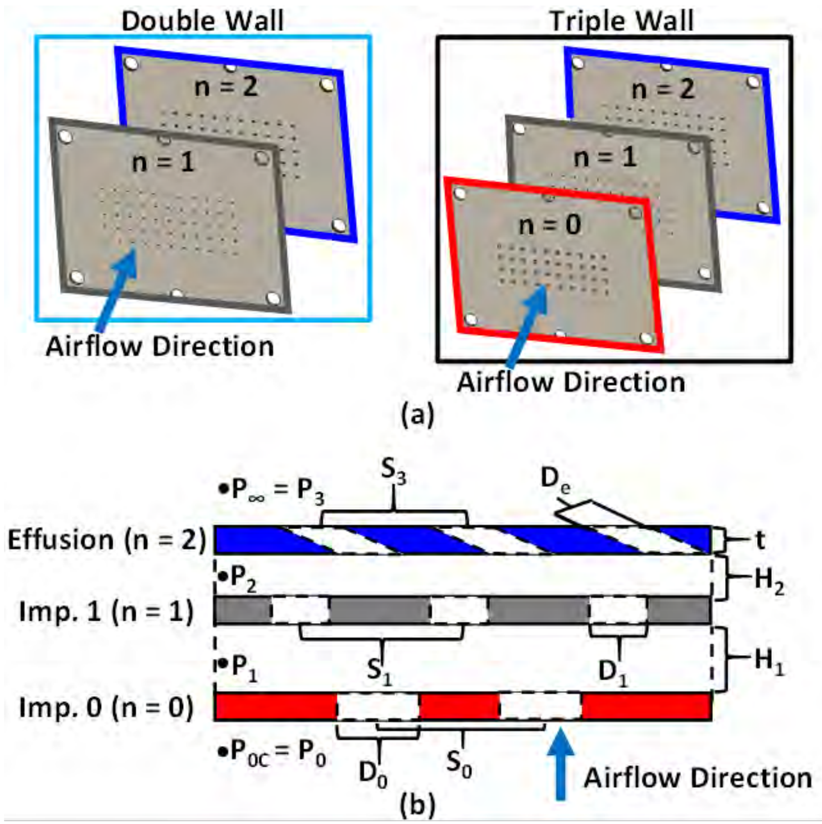

Figure 15. (a) Side view of a double-walled and triple-walled liner used for dirt mitigation studies. (b) Side view of a triple-walled liner including pressure ratio definitions.

Table 1. Triple-walled Liner Parameters.

	H/d	t/d	α	Pressure Split (%)
Imp-125	10	1	0.08	0.1
Imp-09	10	1	0.042	0.4
Imp-06	10	1	0.019	2.0
Imp-025 Pins Diamond Fence	3	2	0.018	17
Eff-033	N/A	2	0.005	82

$$\alpha = \frac{\text{Impingement Flow Area}}{\text{Total Flow Area}}$$

$$\frac{t}{d} = \frac{\text{Plate thickness}}{\text{impingement diameter}}$$

Pressure correlations were utilized to develop flow areas for each of the plates as well as the plate thicknesses to match previous testing done within the lab. The parameters developed for each of these are shown in Table 1. Imp-125, Imp-09, and Imp-06 refer to the three different diameters tested for the first impingement plate, which were used to analyze the effects of first plate pressure split on deposition, where increased diameters resulted in decreased pressure splits which is shown in Table 1. Pressure split is defined in Equation 6, where it represents each individual plate pressure contribution to the total pressure drop across all 3 plates.

$$\text{Pressure split} = \frac{\Delta P_{\text{individual}}}{\Delta P_{\text{Total}}} * 100 \quad \text{(Eq. 6)}$$

The H/D spacing between Imp-06 and Imp-025 was set at 10, while the H/D ratio between the Imp-025 and Eff-033 was set at 3. This decision was made based on previous testing (McFerran et al., 2025) which showed that as H/D increased, dirt was more likely to be captured on the plate. Because the goal is to increase capture on imp-025 and decrease capture on eff-033, a larger H/D was chosen for Imp-06 than Imp-025.

The 4 x 10 array dimensions for Imp-06 differed from the 5 x 11 array dimensions of the other two plates because the impingement jets from Imp-06 were designed to impact in the center of the Imp-025 cooling holes, which can be seen in Figure 16. Designing the impinging jets in the center was done to keep the dirt as far from each of the Imp-025 cooling holes as possible. Ultimately, deposition on Imp-025 is not as big a detriment to the combustor wall as deposition on Eff-033 because Eff-033 is the plate that needs maximum cooling due to high temperature exposure.

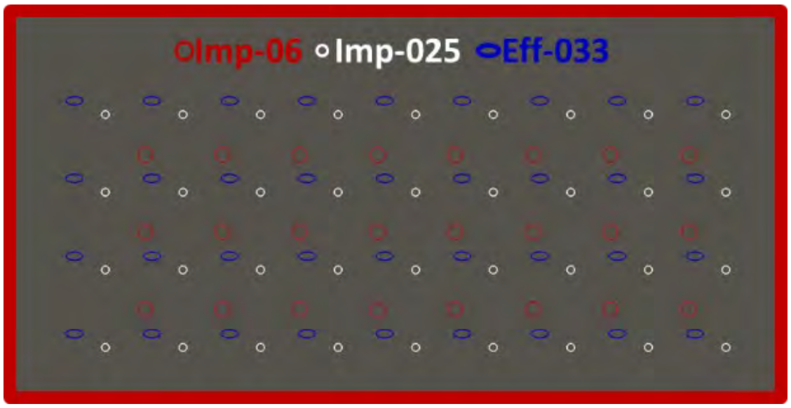

Figure 16. Top-down view of the impingement and effusion holes locations for each layer.

Geometric surface structures were also designed on the Imp-025 surface with the goal of capturing more dirt on this layer than Eff-033. The four designs of surface structures tested (i.e., pins, diamonds, fence, and tall fence) are shown in Figure 17b. For each of these designs, the Imp-06 plate was used as the first layer impingement plate. The goal of the pin design was to block a direct flow of the impinging jets from Imp-06 to the cooling holes of Imp-025. Without a direct path to the hole, the dirt would be more likely to deviate from the flow field path and not funnel into the holes. The diamond and fence designs were designed to cause a sharp velocity gradient at the base of a wall in which the flow would need to go up and over because past studies (Fallon et al., 2023; Singh et al., 2013; Lundgreen, 2017) have shown that particulate has a difficult time following flows with sharp velocity gradients. The pin and diamond designs had heights equal to a quarter of the plate-to-plate spacing between Imp-06 and Imp-025, while the fence and tall fence designs were 1/6th and 1/3rd of the plate-to-plate spacing, respectively. A side view in Figure 17a shows the height of the pins compared to the plate-to-plate spacing.

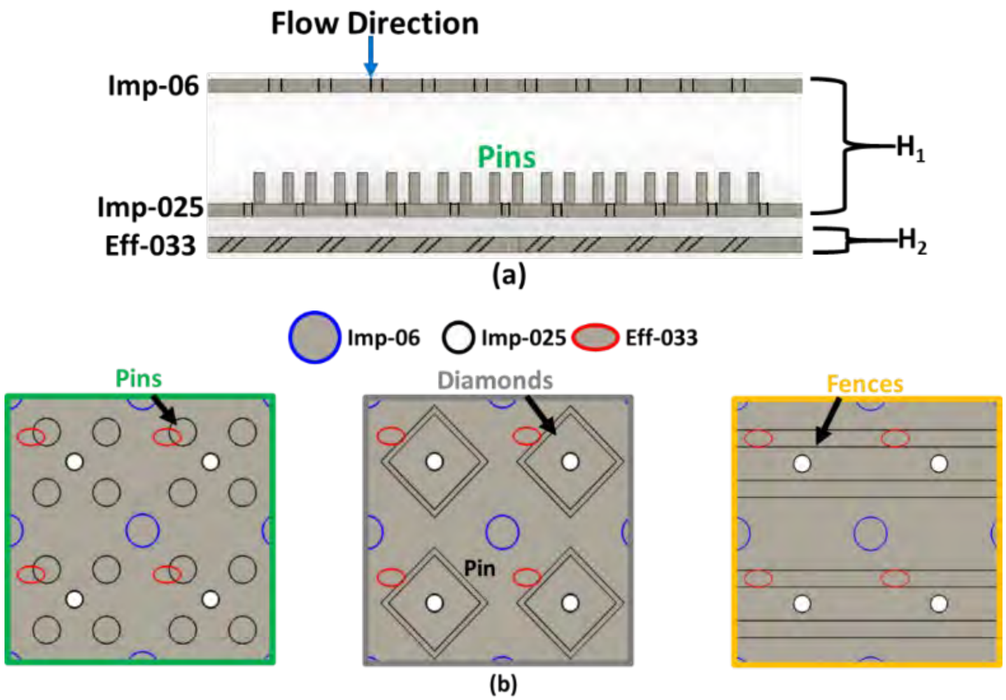

Figure 17. (a) Sideview of the pin design on Imp-025 where H_1/D equals 10 and H_2/D equals 3. (b) Top view of the four different designs tested on Imp-025. Note that two different fence heights were tested for the fence design.

Prior to each test, the mass of each layer of the triple-walled liner was recorded and assembled at the base of the plenum. Clean pressure and FP measurements were made on each clean layer to obtain the clean test conditions. Dirt was then injected via a slug feed method discussed in previous quarters, causing dirt to deposit on all three layers of the combustor liner. After injection, pressure and FP measurements are once again taken and the entire rig was disassembled. Upon disassembly, each of the layer's masses were measured and the differences in mass between the dirty (mf) and clean (m0) plates gave the mass of dirt on each layer.

First, the effects of first plate pressure split were analyzed for the 3-layer composites by adjusting the diameters of the first plate impingement holes (Imp-06, Imp-09, or Imp-125). A pressure split of 2% PR, 0.4% PR, and 0.1% PR were tested for Imp-06, Imp-09, and Imp-125, respectively, where PR was equal to 1.045 across the entire assembly for both double-walled and triple-walled testing. Results for the percentage of dirt captured per layer are shown in Figure 18 for both the 2-layer and 3-layer walls. For each of these tests, 2.0 g of dirt was injected. As the pressure split across the first plate increased, the percentage of dirt found on the Imp-025 plate compared to that on Eff-033 also increased. For the Imp-06 plate which had a 2% PR pressure split, only 17% of the total dirt distribution ended up on the effusion plate, which is an 83% reduction in deposition compared to the 2-layer design. Even Imp-125 performed very well, resulting in more than a 50% reduction in the Eff-033 deposition while only contributing 0.1% to the total pressure ratio.

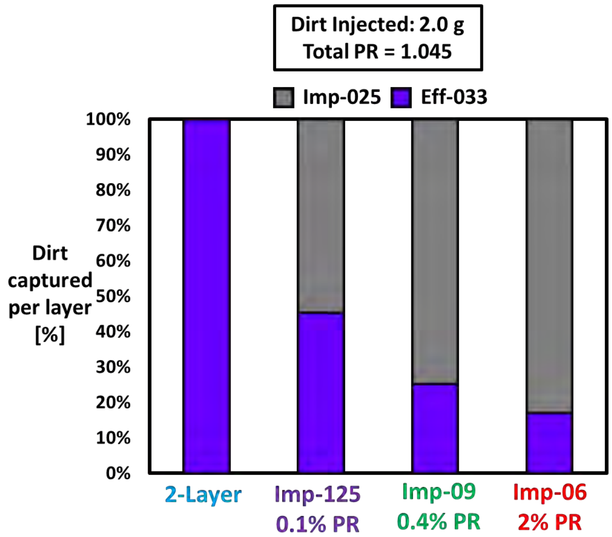

Figure 18. Percentage of dirt captured on Imp-025 and Eff-033 for Imp-125, Imp-09, and Imp-06 as the first (cold-side) liner.

The RFP was also analyzed as a function of % PR for each of these three designs, as shown in Figure 19. As the % PR increased across the first impingement plate, the RFP decreased, which means that there was less overall flow blockage as the first plate pressure split increased. Therefore, as the % PR increased, the RFP and deposition mass on Eff-033 decreased. This trend suggests that the effusion plate is the layer that has the greatest impact on flow blockage because the flow blockage decreased as deposition on the effusion plate decreased. Experimental observations of the deposition patterns also support this trend, as dirt buildup in the holes was visualized during testing.

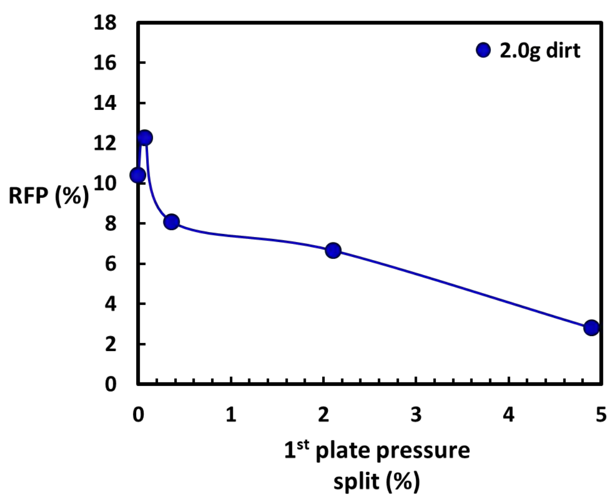

Figure 19. The reduction in flow parameter as a function of first plate pressure split for an injection of 2.0 g of dirt at a total pressure ratio of 1.045.

An analysis of the individual pressure splits before and after dirt injection, as seen in Figure 20, show that the pressure split across Eff-033 increased as dirt was injected into the system. This result supports the idea that the effusion plate contributes the most to the total flow blockage because despite a decrease in the mass flow rate, the pressure split across this plate increased. The only way for this to happen is if the flow area on this plate decreased which would indicate flow blockage. Also, in Figure 20, the clean PR across each of the plates shows the increase in PR across the first impingement plate as the diameter of the holes were decreased.

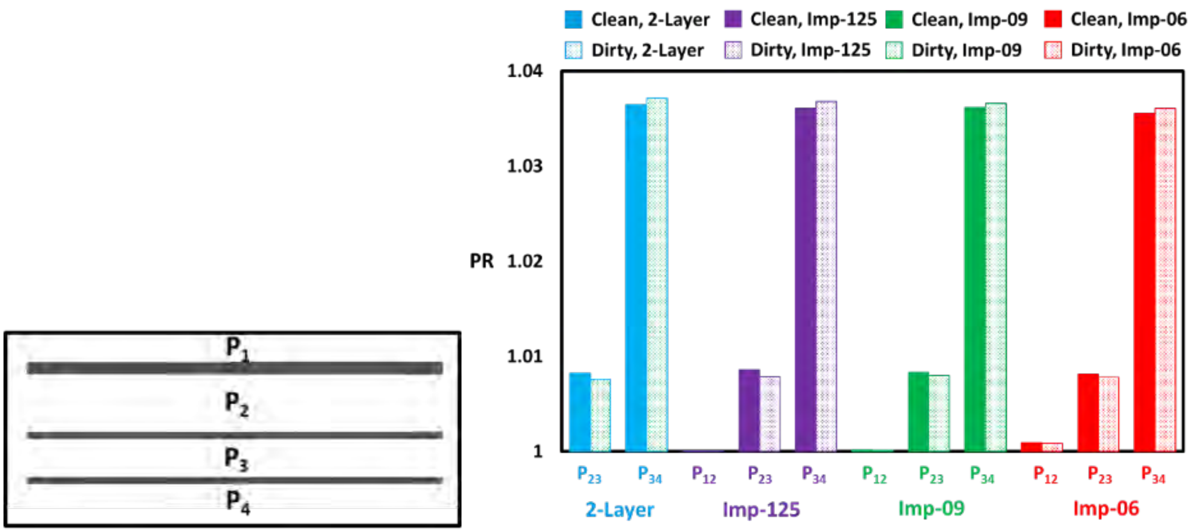

Figure 20. Pressure splits across each of the liner walls for the 2-layer and 3-layer designs used to analyze the effects of first plate pressure splits.

Any pressure split across the first impingement plate is a pressure loss, which reduces efficiency because more cooling air would be needed to effectively cool the effusion wall. However, as this pressure split increased, the deposition mass on Eff-033 and the RFP decreased. As a result, it is important to consider how the benefits of increased dirt reductions can outweigh the negative impacts of increased pressure losses, especially considering the significant impact dirt deposition has on cooling as seen in previous quarters (McFerran et al., 2025).

The Imp-06 plate was chosen as the first impingement plate for the rest of testing because it resulted in the greatest reductions in deposition on the effusion plate compared to Imp-09 and Imp-125. The next set of tests studied the effects of dirt injection on deposition distributions, where injection masses of 0.5 g, 1.0 g, 1.5 g, and 2.0 g were evaluated. Studying different injection masses was also useful in quantifying the benefits of a triple-walled liner over time because deposition increases over time in an engine. It was found that capture percentages for the Imp-025 and Eff-033 layers were insensitive to injection mass, as seen in Figure 21. At each of the tested injection masses, the percent of dirt captured on Eff-033 compared to Imp-025 ranged between 17-20%.

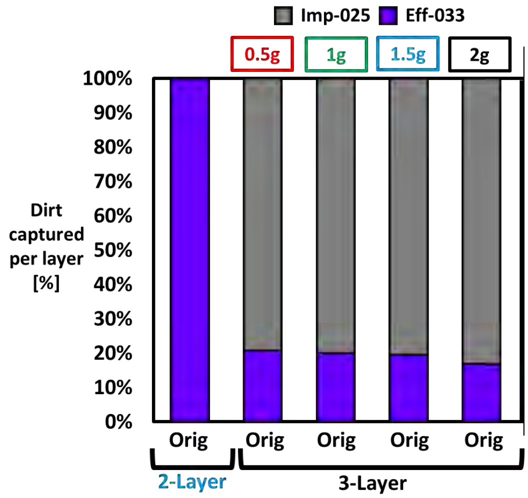

Figure 21. The percentage of dirt captured on the baseline 2-layer and 3-layer designs with injection masses between 0.5 and 2.0g.

Although not shown in a plot, the individual pressure splits once again demonstrated that the effusion plate pressure split increased as dirt was injected into the system, despite a reduction in the flow parameter. This change in pressure split for the effusion plate increased as the dirt injection mass increased, and this is a result of the increase in RFP that occurred as the injection mass increased, as shown in Figure 22. These results are shown for both the 2-layer and 3-layer designs. As the injection mass increased, the RFP increased for double and triple-walled liners because with more dirt, there is inherently a greater likelihood of flow blockage. However, the RFP for the 3-layer design was 40% less than that for the 2-layer design at the same injection mass. These results further support the idea that the effusion plate is the main driver of RFP because the deposition mass on Eff-033 was less for the 3-layer design than the 2-layer design, so a decrease in the RFP would also be expected.

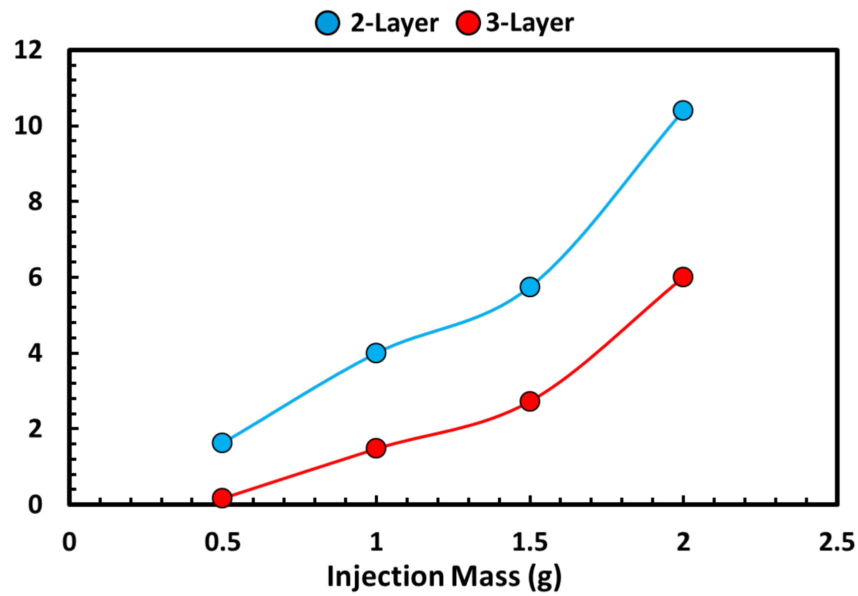

Figure 22. Reduction in Flow Parameter for the baseline 2-layer and 3-layer designs as a function of dirt injection mass.

Finally, the feature designs introduced in Figure 16 were added to the Imp-025 plate with the goal of further enhancing dirt capture on this layer as opposed to Eff-033. The dirt capture per layer is plotted in Figure 23, which compares the four designs (i.e., pin, diamond, fence, and high fence) to the 2-layer baseline and 3-layer baseline. Each of these tests were performed with 2.0 g of dirt injection at a PR of 1.045. Results in Figure 23 show that the pin and diamond designs reduced deposition on the effusion plate by 5% compared to the 3-layer design with the regular Imp-025 plate. In contrast, the fence and high fence designs performed 1-2% worse than the 3-layer with regular Imp-025 in terms of deposition distribution on the effusion plate.

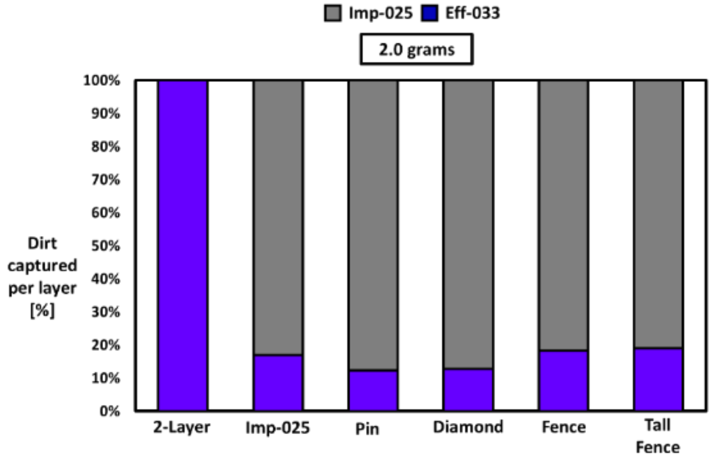

Figure 23. The percentage of dirt captured on Eff-033 and Imp-025 with the pin, diamond, fence, and tall fence designs for an injection mass of 2.0g and PR of 1.045.

Despite having slight differences in dirt distribution among the different layers, the RFPs for the pins, diamond, fence, and tall fence designs were slightly less than that for a 3-layer with the regular Imp-025 plate as shown in Figure 24. However, the high fence had an RFP about 25% higher than any of the other structural designs. The effusion plate was once again the main driver of this RFP. Experimental observations of the deposition patterns in Figure 25 show some of the dirt buildup occurring in the effusion holes which contributes to flow blockage. Additionally, these microscopic images show the deposition patterns on the imp-025 plate for each of the designs. The deposition patterns have similar characteristics to patterns seen previously, where conical mounds form in the regions of direct impingement.

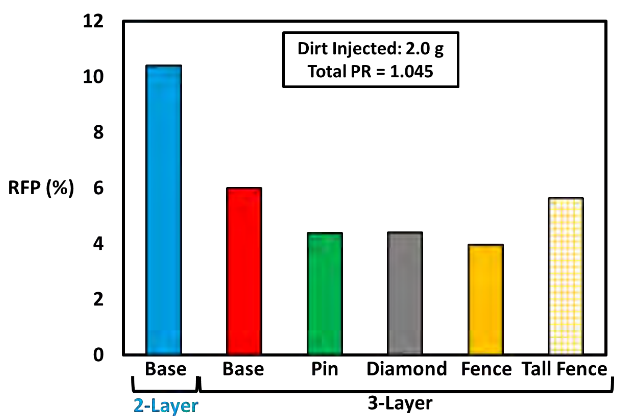

Figure 24. RFP for the 2-layer and 3-layer baseline and structural designs.

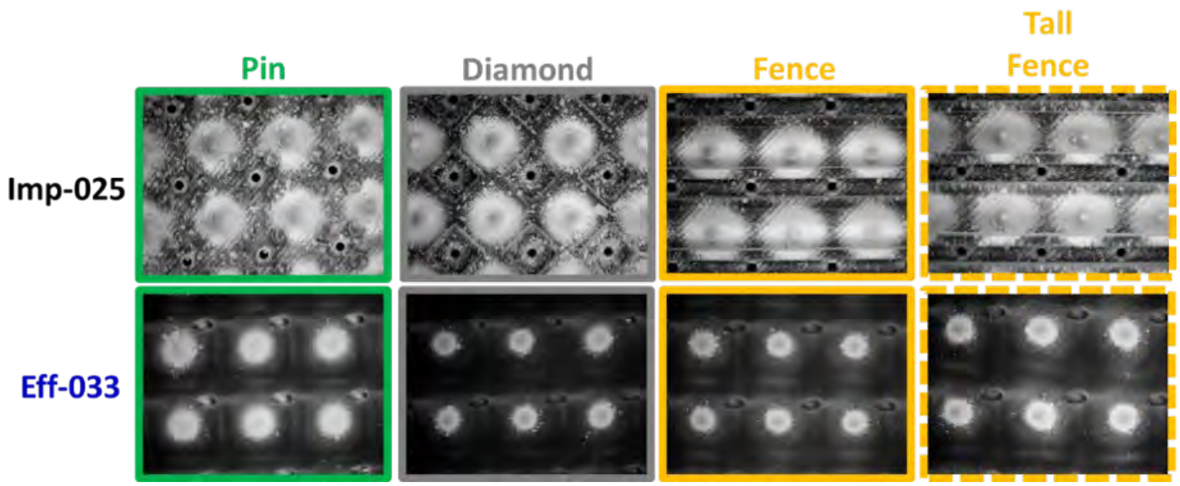

Figure 25. Deposition patterns on the Imp-025 and Eff-033 plates for each of the structural designs evaluated.

Also, during this past year, there was a focus on the effects of different particle sizes and different dirt compositions to see whether the triple wall remains effective for these conditions. Figure 26 show the effect of particle size using the US Air Force Research Laboratory (AFRL)-05 (original) test dirt by expanding the largest particle diameter from 1 μm to 10 μm. As already discussed, for the double wall, it is expected that 100% of the dirt is deposited on the effusion plate. The results in Figure 26 show that, similar to those of the 1 μm particle that the triple wall is still effective.

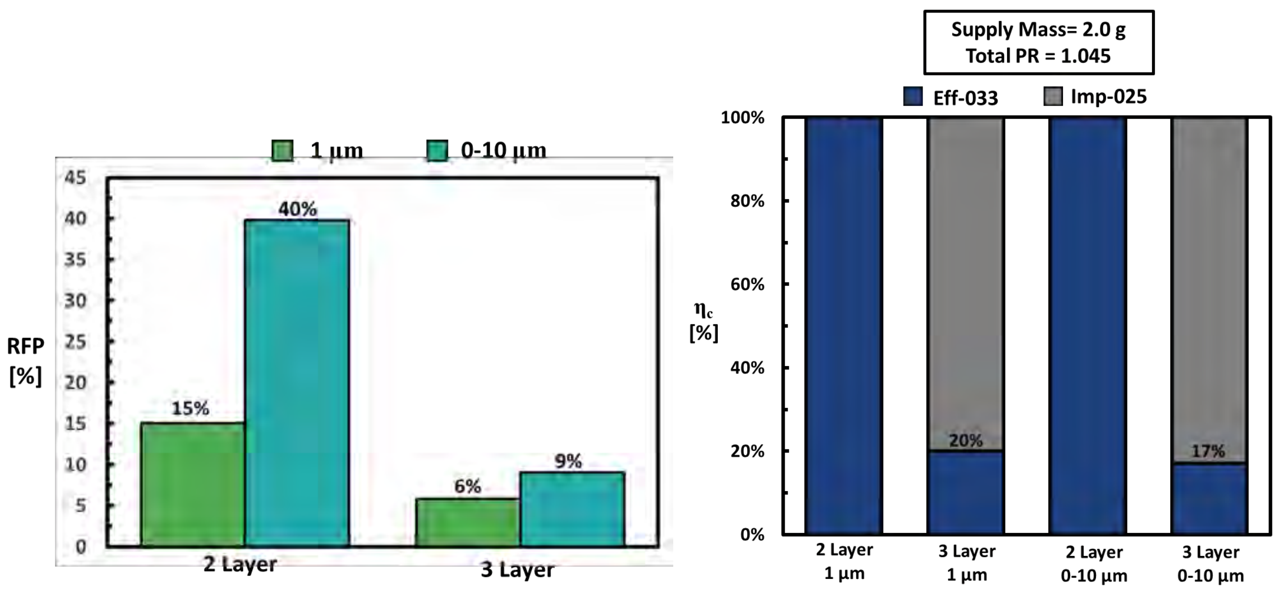

Figure 26. Comparison of capture efficiency and reduction in flow parameter for two different particle sizes using the AFRL-05 test dust.

Also shown in Figure 26 is that the reduction in flow parameter also was reduced, meaning that more flow resulted when using the triple-wall due to less flow blockage even when the particle size increased. However, it is important to note that for both the double- and triple-wall designs the overall RFP increased, indicating that the larger particles had a tendency to block the cooling holes more readily as expected. Figure 27 shows images on the effusion plate of these blockages comparing the smaller and larger particle size tests.

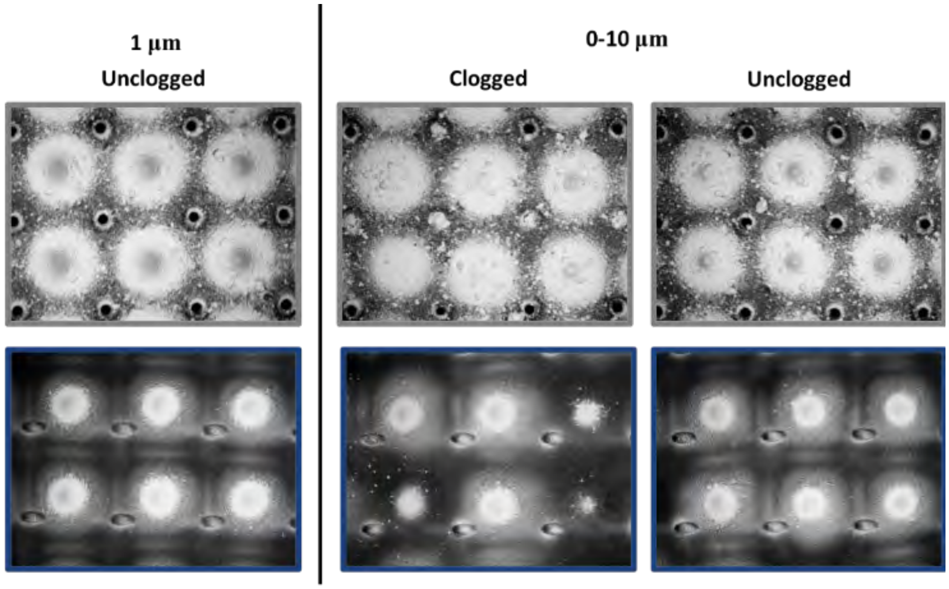

Figure 27. Comparison of deposition patterns for two different particle sizes using the AFRL-05 test dust.

One of the simplified tests that was conducted during this reporting period was also to heat the dirt to temperatures relevant to turbine conditions. Based on the data shown in Figure 28, there is a dramatic effect of temperature especially when nearing turbine operating temperatures. These results indicate the importance of testing at relevant temperatures.

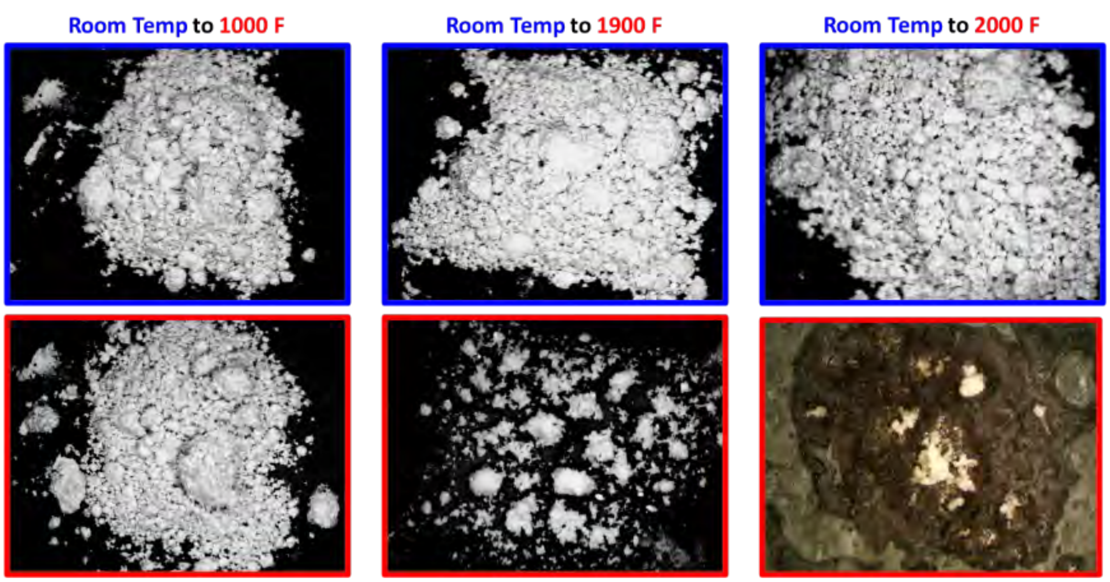

Figure 28. AFRL-05 test dust as a function of exposure temperatures.

In summary, a triple-walled liner was developed in which an impingement plate was added upstream to a typical double-walled liner. It was shown that the inclusion of this plate can lead to reductions in dirt deposition on the effusion plate because more of the dirt deposits on the middle impingement plate, which acts as a sacrificial filter. With there not being a strong need to cool this middle plate, deposition on this surface is not that significant compared to deposition on the effusion plate. Testing was performed for several % PRs across the first impingement plate, dirt injection masses, and structural designs. Overall, the reduction in deposition on the effusion plate also led to decreased reductions on the cooling flow due to dirt blockage, which is another benefit of the 3-layer design. It was also shown that the no matter the particle size, there was an improved performance of reduced impacts on the external effusion hole wall.

Task 3 – Profile Simulator for START

The Pennsylvania State University

Objectives

The objective of this task is to (1) develop and integrate a non-reacting profile simulator to be placed upstream of the START test turbine, and (2) understand the impacts of a range of temperature and pressure profiles, representative of current and future combustors, on turbine efficiency and durability.

Background

The ability to replicate combustor-relevant temperature and pressure profiles is important in learning how to improve engine performance with typical aviation fuels, sustainable aviation fuel, and other fuels. These profiles, which exit the combustor that then enter the turbine, impact turbine efficiency and durability. This task involves developing a non-reacting profile simulator that can simulate relevant combustor non-dimensional flow and thermal fields. Figure 29 illustrates the need for placing a combustor simulator upstream of the START test turbine. The data in Figure 29 show the range of nonuniformities of non-dimensional temperatures ($\overline{T}/T_m$) that occur at the exit of the combustor, which affects turbine performance. The profiles labeled “Engine Profile 1” through “Engine Profile 4” are from Barringer et al. (2004) and show a variety of combustor exit profile shapes influenced by liner wall dilution and effusion flows. Five additional profiles are shown for comparison including “Engine Profile 5” and “Engine Profile 6” obtained from gas turbine OEMs (OEM Engineer Manufacturers, 2022), an OEM engine profile (“Engine Profile 7”) from Karalus et al. (2019), a typical engine profile (“Engine Profile 8”) from Povey et al. (2007), and a final profile showing the current START facility inlet temperature profile for the National Experimental Turbine (NExT) that is nearly uniform. Because various fuels will be used for combustion in the future, simulating these profiles will become even more essential.

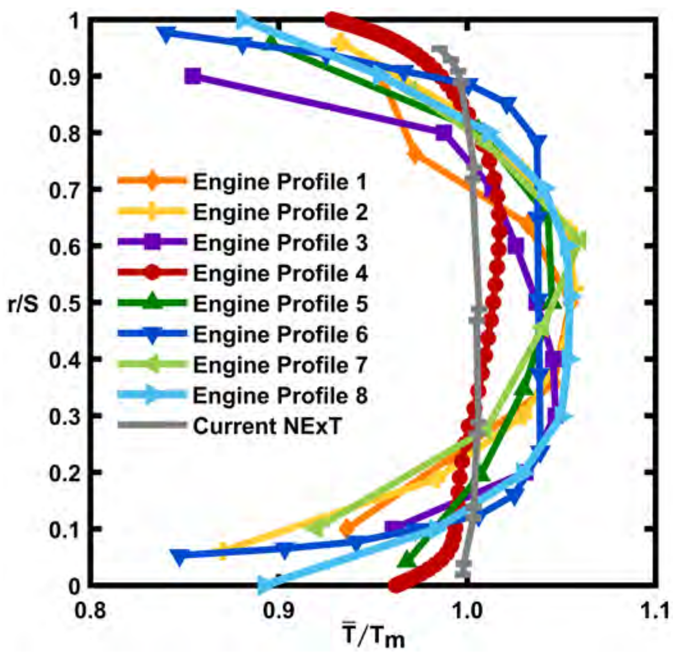

Figure 29. Combustor exit profiles from the literature, indicating non-uniform temperatures ($\overline{T}/T_m$).

A combustor profile simulator is being designed and implemented into the START rig upstream of the turbine test section. The purpose of the simulator is to replicate the temperature and pressure profiles at elevated turbulence levels that are characteristic of the flow exiting a modern gas turbine combustor. A number of generalized temperature profile shapes are being targeted for the design including a radial mid-span peaked, outer diameter (OD) peaked, inner diameter (ID) peaked, and a flat uniform profile. The simulator device consists of a series of solid and perforated walls that form a central chamber, similar in concept to a gas turbine engine combustion chamber.

To achieve the range of temperature and pressure profiles, our team conducted predictive computational fluid dynamics (CFD) simulations using steady Reynolds-averaged Navier–Stokes to understand the impacts of different flow features on the resulting profiles. Simultaneously, the START team engaged a design firm to develop the hardware necessary to achieve the profiles developed through the CFD studies.

Recall, the central chamber of the simulator design includes three axial rows of dilution holes and several rows of effusion holes in both the inner and outer diameter liner walls. The first dilution row is used for turbulence generation, whereas the second and third dilution rows are used for temperature profile generation. The effusion flow is used to tailor the temperature in the near-wall regions. The dilution holes will be drilled into the annular walls, which are removable to allow different dilution hole diameters and corresponding momentum flux ratios to be studied.

The domain of the CFD simulation began at the axial inlet of the central chamber and ended at the turbine vane leading edge. The flow inlets for the simulation domain included the main gas path central chamber inlet, approach flow plenums for the dilution holes, and effusion zone liner walls. All of the flow inlets were designated as mass flow inlets, including the approach flow paths leading to the dilution holes, which provided more realistic flow interactions between the dilution jets and mainstream crossflow. The temperature of the first-row dilution jets was set to match the temperature of the flow at the main gas path inlet in order to maintain the majority of the total flow at an elevated temperature level above the second/third row dilution flow and effusion flow. This elevated flow temperature, illustrated in Figure 30 by the red colored flow vectors, helps to produce a mass-averaged flow temperature at the turbine vane inlet plane that matches the design target for conducting the turbine experiments. The temperature of the second/third row dilution flow is illustrated at a lower temperature level in orange, and finally the effusion flow is illustrated at an even lower level in blue. Overall, the three levels of flow temperatures are used to establish the target mass-averaged flow temperature entering the turbine vanes. The turbine vane inlet was set as a pressure outlet boundary condition, defined using the static pressure at the turbine vane leading edge. All of the boundary conditions are summarized in Figure 30.

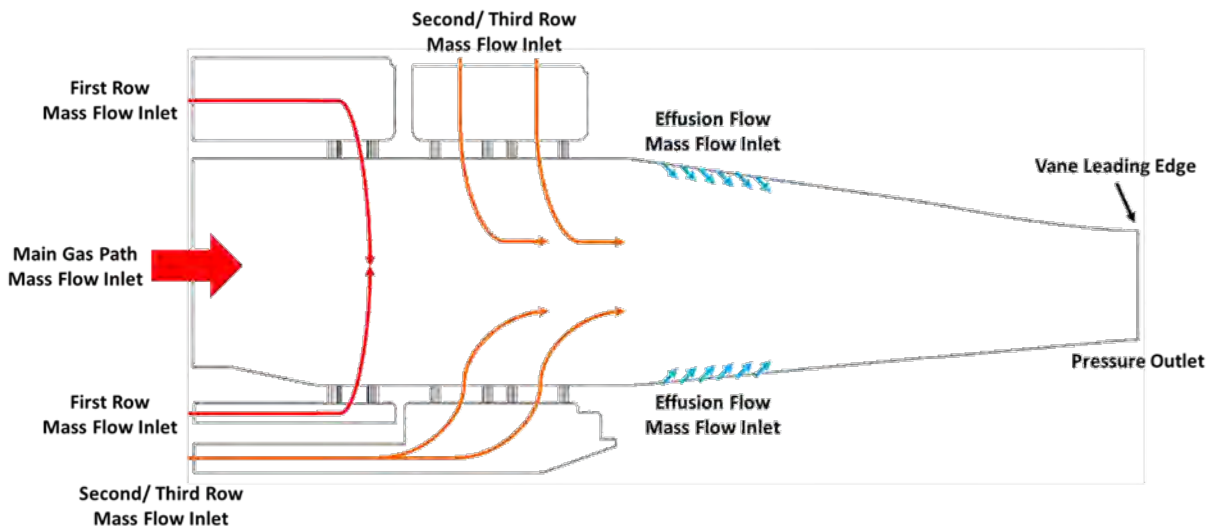

Figure 30. Diagram of boundary conditions used for the SimCenter®-STAR CCM+[1] CFD simulations.

® SimCenter is a registered trademark of Siemens Industry Software N.V., Leuven. Belgium.
[1] SimCenter STAR CCM+ is a multiphysics CFD software that models complex fluid dynamics applications for real-world conditions including single-phase, multiphase, reacting, heat transfer, aeroacoustics, and fluid-structure interaction simulations.

Profile Simulator Results

The setup work for CFD simulations, including mesh generation and a grid independence study, and the execution of the CFD simulations were completed during Q3 and Q4 of 2023. Two different 2-level fractional factorial Design of Experiments (DoE) were completed. The second DoE included four more additional factors than what was included in the first DoE. The 12 factors as part of the second DoE are shown in Table 2 and included (1) dilution row 1 mass flow rate, (2) dilution row 1 hole diameter, (3) dilution row 3 OD mass flow rate, (4) dilution row 3 ID mass flow rate, (5) effusion flow OD mass flow rate, (6) effusion flow ID mass flow rate, (7) dilution row 3 OD hole diameter, (8) dilution row 3 ID hole diameter, (9) dilution row 3 OD total temperature, (10) dilution row 3 ID total temperature, (11) effusion flow OD total temperature, and (12) effusion flow ID total temperature. The second CFD design of experiments allowed more variables to be studied in order to generate a wider range of profile shapes. Since both DoEs were a 2-level design, the maximum and minimum of the respective ranges were used for the hole diameters and mass flow rates. The changes made to the first-row dilution flow and holes described by the first two factors were to understand the effects of turbulence on the profile shape. The remaining ten factors were changed to study their effects on the exit temperature and pressure profile shapes.

Table 2. Factors for the 2-level, 12-factor fractional factorial DoEs.

Factor Number	Input factors	Lower Level	Upper Level
1	$\dot{m}_1/\dot{m}_t$ [%]	0.18	0.22
2	D_1/S [-]	0.23	0.45
3	$\dot{m}_{3,\,OD}/\dot{m}_t$ [%]	8.8	11
4	$\dot{m}_{3,\,ID}/\dot{m}_t$ [%]	8.8	11
5	$\dot{m}_{e,\,OD}/\dot{m}_t$ [%]	3.8	6.3
6	$\dot{m}_{e,\,ID}/\dot{m}_t$ [%]	3.8	6.3
7	$D_{3,\,ID}/S$ [-]	0.39	0.55
8	$D_{3,\,OD}/S$ [-]	0.39	0.55
9	$T_{3,\,OD}/T_m$ [-]	0.55	0.75
10	$T_{3,\,ID}/T_m$ [-]	0.55	0.75
11	$T_{e,\,OD}/T_m$ [-]	0.55	0.75
12	$T_{e,\,ID}/T_m$ [-]	0.55	0.75

The non-dimensional temperature profiles predicted by the simulations at the exit plane of the combustor profile simulator for the second CFD design of experiments are shown in Figure 31 for the grid-independent 20 million cell mesh.
The shapes of the engine profiles are mostly in the profile range capability predicted by CFD simulations. The shaded gray region of Figure 31 represents the range of profiles that correspond to the DoE case configurations. The short-dashed black lines represent individual CFD DoE case profiles. The steepest wall gradients characteristic of Engine Profile 3 and 6 were not captured by the second DoE test matrix. However, this does not mean that the simulator is not able to produce temperature profiles with steeper gradients along the walls. Steeper gradients might be possible since the CFD DoE only varied 12 factors that had settings of the minimum or maximum within their selected ranges and did not encompass all the factors as part of the simulator's flexibility.

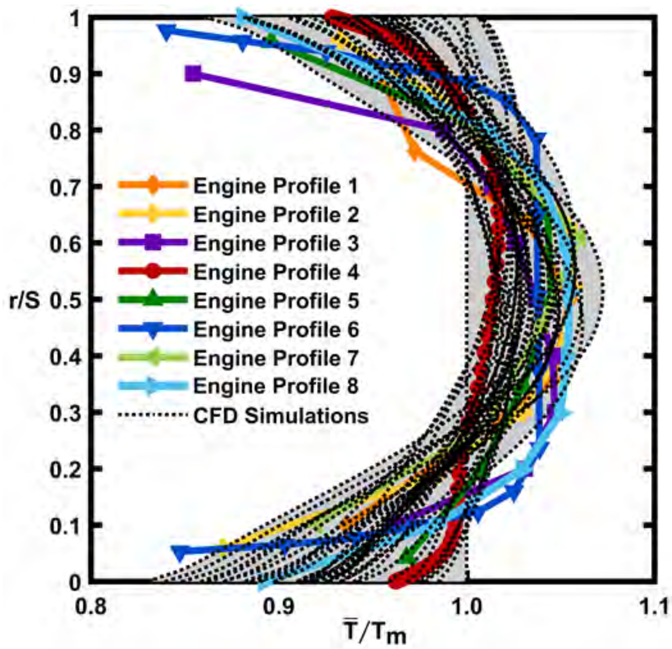

Figure 31. Several non-dimensional total temperature profiles at the simulator exit from the second CFD design of experiments, plotted in the radial span direction (r/S) and circumferentially averaged, with comparisons to typical engine profiles.

Recall, the design targets for the new profile simulator include a radial mid-span peaked, OD peaked, ID peaked, and a flat uniform profile. The profile results from the second CFD design of experiments that best matched the design targets were selected and plotted in Figure 32 for easier visibility. The four simulation-predicted profiles shown in Figure 32, designated as 'Center Peaked', 'ID Peaked', 'OD Peaked', and 'Uniform', are more representative of the engine profiles than what was previously found in the first CFD design of experiments using a 2-level 8-factor approach. The shaded gray region in Figure 32 is the same as that shown in Figure 31, which represents the full-range of profiles produced by the second CFD DoE.

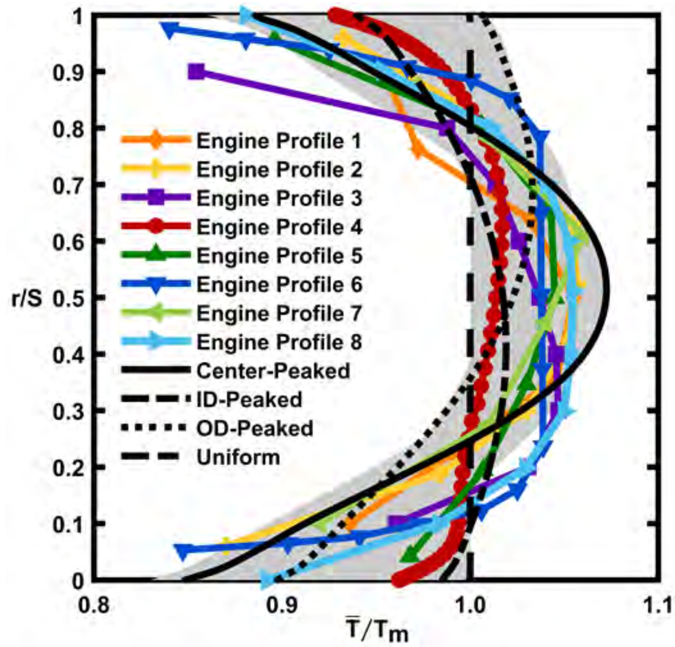

Figure 32. Range of non-dimensional total temperature profiles from the second CFD design of experiments, plotted vs. radial span location and compared to the example engine combustors.

A sensitivity analysis was completed during the current reporting period on the profile results from the second CFD DoE to understand how each of the 12 input factors affect the exit temperature shape. The sensitivity analysis determines which factors significantly affect the profile shape so that targeted profiles can be produced. An analysis of variance (ANOVA) was conducted on the predicted exit profile shapes at eleven discrete radial locations that correspond to the measurement locations of the traverse system probes in the START rig. However, only three radial locations—10%, 50%, and 90% radial span—are presented to illustrate the importance of the sensitivity analysis. The ANOVAs conducted allowed the percent contribution of each input factor to be calculated for each of the 11 radial span locations. The percent contributions of each factor to the temperature profile shape were determined by calculating the ratio of the individual factor's sum of squares to the total sum of squares. The individual factor's sum of squares refers to the variation in the non-dimensional temperature at a specific radial span location that can be contributed to that factor, while controlling the other factors. The total sum of squares is the sum of the individual factors sum of squares within a particular ANOVA. The percent contributions for each of the 12 factors at 10%, 50%, and 90% span can be seen in Figure 33. The largest, secondary, and tertiary contributors to the profile shape at 10% span was the injection temperature the ID effusion flow, the injection temperature of the ID third-row dilution flow, and the mass flow rate of the ID effusion flow, respectively. At 50% span the first-row dilution hole diameter was the largest contributor and was significantly higher than the rest of the contributors. The largest, secondary, and tertiary contributors to the profile shape at 90% span were the injection temperature of the OD effusion flow, first-row dilution hole diameter, and injection temperature of the OD third-row dilution flow, respectively. The percent contributions of the injection temperature of the OD third-row dilution flow and mass flow rate of the OD effusion were very close in being the tertiary contributor at 90% span. However, based on the 36 simulations that were part of the ANOVA, the injection temperature of the OD third-row dilution flow had a slightly higher percent contribution when compared to the mass flow rate of the OD effusion flow. This is similar to the percent contributions at 10% where the injection temperature of the ID third-row dilution flow had a higher contribution than the mass flow rate of the ID effusion flow. The largest contributors for 10% and 90% radial span intuitively make sense since the effusion flow is designed to blanket the chamber walls. The first- and third-row dilution flow do not mix effectively with the effusion flow at low and high radial spans leading to a large contribution of the effusion temperatures. At 50% span, the first-row dilution hole diameter has a large effect on the turbulence generated. For a case when the turbulence in the simulator is high, the hot flow of the main gas path and first-row dilution mix well with the colder third-row dilution flow. As the flows mix, the bulk average exit flow is lower when compared to a case with low turbulence levels. For a low turbulence case, the flows do not mix comparatively as well, allowing hot main gas path and first-row dilution flow to continue downstream creating a hot mid-span peak in the temperature profile.

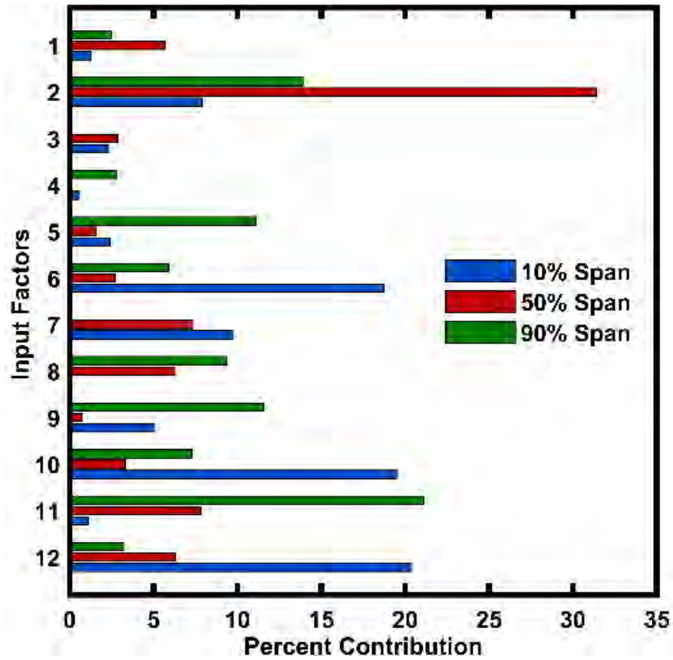

Figure 33. Results from the second DoE sensitivity analysis for (a) 10% span, (b) 50% span, and (c) 90% span, illustrating the impact of individual factor effects on the exit temperature profile metric $\overline{\mathrm{T}}/\mathrm{T_m}$.

One reason for the selection of the four target profiles was to allow the target profiles to be studied in depth using a higher fidelity computational model and experiments. It was previously determined that the Reynolds-averaged Navier Stokes (RANS) model provides a good prediction of the flow physics, such as jet penetration depth and bulk averaged velocities, but large eddy simulation (LES) modeling is needed to accurately capture the turbulence created by the mixing process of the dilution jets. Understanding how well the RANS simulations predict the temperature profiles is important in determining the viability of using RANS as a predictor for the various flow and geometry configurations in which the profile simulator can be installed and operated. The center-peaked target profile was selected as the preliminary case to transition to LES modeling.

Prior to a transition from RANS to LES, a more in-depth RANS simulation (REV-7), was completed that included the domain regions defined by the upstream strut, profile plate, and downstream turbine vane. The turbine vane used is from the PSU NExT geometry. This updated CFD domain can be seen in Figure 34, with the axial location of the turbine inlet traverse rakes marked in green and axial location of the vane leading edge (LE) marked in blue. The perforated profile plate acts to reduce the air pressure to enable proper injection of the dilution and effusion flows into the central chamber. The profile plate is interchangeable and contains an engineered perforated pattern that facilitates the desired air mass flow distribution throughout the simulator. In addition to creating a pressure loss, the profile plate is used to reduce the aerodynamic wake effect of the strut's presence in the main flow and to create a uniform flow field entering the central chamber. The struts function as a passageway to distribute cooling air to the inner diameter annulus flow paths and to structurally support the inner hardware components.

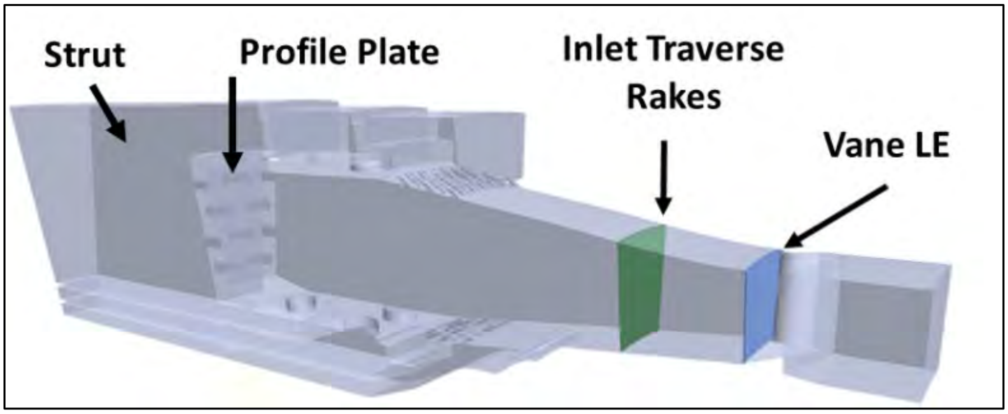

Figure 34. Combustor simulator CFD domain including the upstream strut region, profile plate, and downstream turbine vane (NExT).

The results of the RANS simulation were very encouraging. Figure 35 compares the non-dimensional radial temperature profiles for the 'center-peaked' target profile using the REV-7 simulation domain to the REV-6 domain. Comparisons are shown for axial locations aligned with the vane LE and with the turbine inlet rakes. The REV-7 profile that is axially aligned with the vane LE is not quite as peaked near mid-span (r/S = 0.5) as the REV-6 profile that is also aligned with the vane LE. This slight difference in peak shape is likely attributed to including the NExT vane in the simulation for the REV-7 case, in that the vane's presence had an effect on the flow and thermal fields. The CFD results were extracted at the inlet rake location because this is where physical rakes will be located when the simulator is installed in the rig. Four rakes will measure the air pressure and temperature in the annulus across the full 360˚ circumferential direction. The experiments will allow the comparison of the predicted radial profiles with what is actually measured in the rig. This comparison is important for validation purposes. The REV-7 profile that is axially aligned with the inlet rakes is further peaked than both the REV-7 profile aligned with the vane LE and the REV-6 profile aligned with the vane LE. This increase in peak shape for REV-7 at the inlet rakes is due to the axial location being further upstream. At locations further upstream, not as much mixing from the turbulence has taken place enabling the hotter flow near the mid-span region to remain intact.

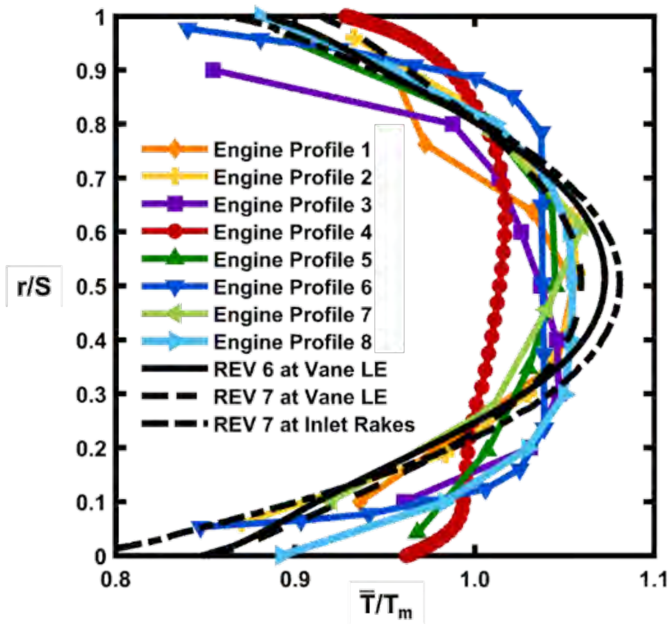

Figure 35. Radial temperature profiles located at the vane leading edge and turbine inlet rakes using the simplified DoE geometry (REV-6) and a more complete geometry (REV-7).

The RANS modeling method used in the CFD DoE study and planned LES modeling method for the higher-fidelity simulations have not yet been validated with experimental results. To validate the modeling methods, both a RANS and LES simulation will be run that uses the same combustor liner geometry as reported by Shrager et al. (2018, 2019). Shrager et al. (2018, 2019) reported flow field measurements and heat transfer performance of the liner wall in the form of overall effectiveness, but overall effectiveness measurements will not be part of the new simulator studies. Therefore, only validation of the computational modeling methods to the flow field measurements will be made. The study performed by Shrager et al. (2018, 2019) presented turbulence levels surrounding the dilution jet, as well as sensitivities to jet momentum flux ratio and freestream turbulence intensity. The outward facing effusion hole geometry as seen in Figure 36 was the selected test case for validation, which includes the highest dilution jet momentum flux ratio of I = 30 and highest freestream turbulence intensity of TI = 13%. This particular case had the most interesting flow phenomena producing a flow field that was significantly different than the other cases. The outward facing effusion hole case formed coherent vortices both upstream and downstream of the dilution jet which can be seen in Figure 37a and Figure 37b.

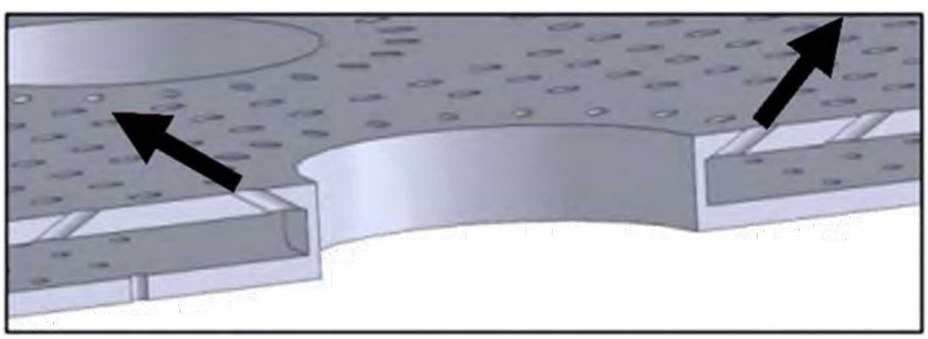

Figure 36. The combustor liner geometry used in the experimental study by Shrager et al. (2018, 2019) showing the large dilution hole with surrounding effusion holes pointing radially outward, that was also used in the current computational simulations to validate modeling methodology.

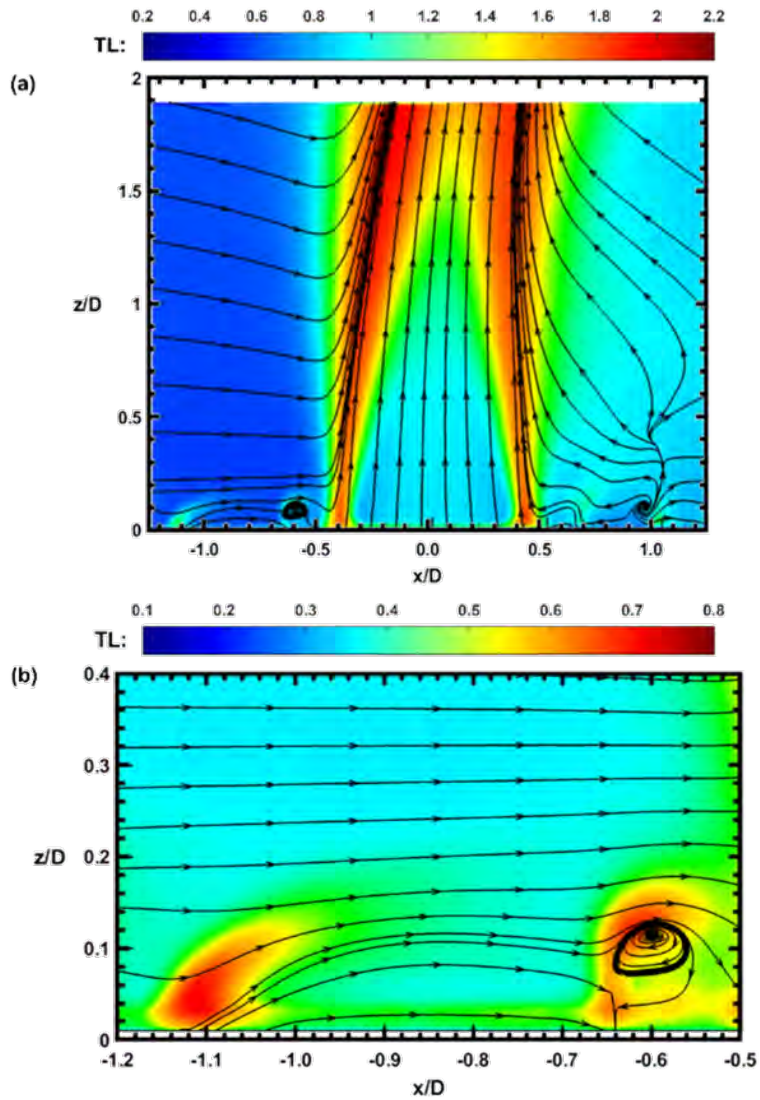

Figure 37. Turbulence intensity contours from experiments by Shrager et al. (2018) for the outward facing effusion hole configuration with a dilution jet momentum flux ratio of I = 30 and a freestream turbulence intensity of TI= 13% showing the flow field (a) near the dilution jet and (b) near the effusion holes.

Five different turbulence models were evaluated to determine the agreement with the experimental results. The five turbulence models that were used included (1) the realizable k-ε model, (2) the k-ω Shear-Stress Transport (SST) model, (3) an incompressible model, (4) a linear pressure strain Reynolds Stress model, and (5) the elliptic blending Reynolds Stress model. The realizable k-ε model is the same RANS turbulence model that was used in the simulator profile simulations. Newly generated turbulence contours with overlaid streamlines are shown in Figure 38a-e from the various turbulence models and compared to the experimental results in Figure 38f. The computational predictions show that the incompressible turbulence model matches well with the realizable k-ε turbulence model. This finding was a good validation check since the flow is well below Mach number 0.1 and can be treated as incompressible. The streamlines in the realizable k-ε simulation and incompressible simulation compare the best to the experimental streamlines. The results from the k-ω SST model, Reynolds Stress with linear blending model, and Reynolds Stress with elliptic blending model all show that the streamlines downstream of the dilution jet do not match well with the experimental streamlines. For all five turbulence models, the turbulence levels are severely underpredicted when compared to the experimental results. This finding is consistent with literature and was not all too surprising. In addition, the jet penetration is underpredicted for all five turbulence models when compared to the experimental results.

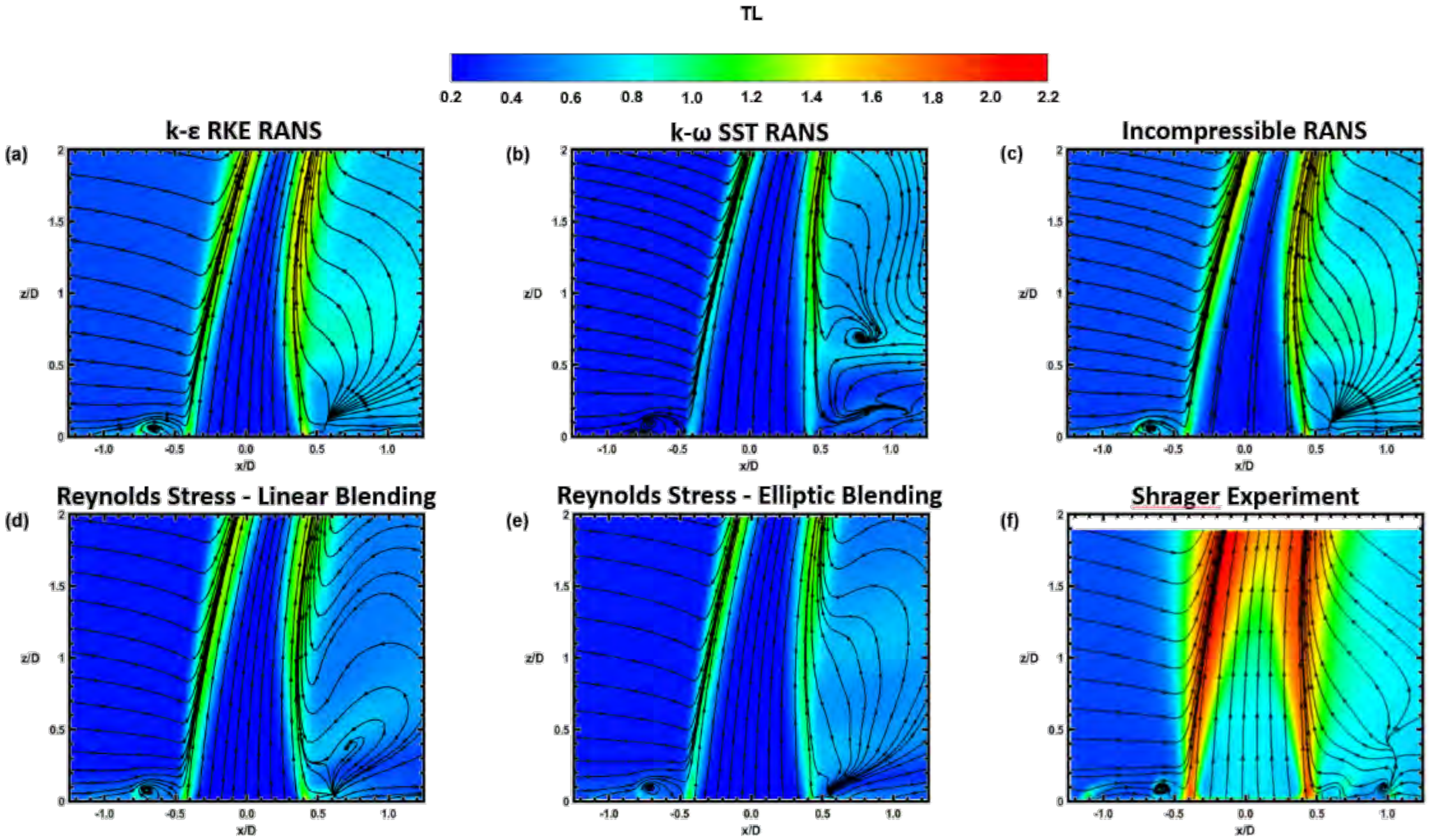

Figure 38. Predicted turbulence intensity contours for the outward facing effusion hole configuration with a dilution jet momentum flux ratio of I = 30 and a turbulence intensity of TI= 13% using the (a) realizable k-ε turbulence model, (b) k-ω SST turbulence model, (c) incompressible turbulence model, (d) Reynolds Stress turbulence model with linear blending, (e) Reynolds Stress turbulence model with elliptic blending, all compared to (f) experimental results from Shrager et al. (2018).

The realizable k-ε predictions compared to the Shrager et al. (2018) experimental results are shown in Figure 39. Figure 39 compares experimentally measured contours of normalized axial velocity, normalized spanwise velocity, and turbulence intensity to the realizable k-ε predictions. When comparing the experimental axial velocity contour shown in Figure 39a to the predicted axial velocity contour shown in Figure 39d, the flowfield upstream of the dilution jet is predicted accurately. The prediction does not compare well with the experimental results inside the dilution jet and downstream of the dilution jet. Within the dilution jet, the axial velocity is overpredicted. This can be explained by the fact that the jet trajectory does not penetrate as far into the mainstream in the computational predictions compared to the experimental results. Resulting from this jet turning, the flow velocity becomes stronger in the axial direction. The spanwise velocity of the experimental results shown in Figure 39b compares adequately with the spanwise velocity of the predicted results shown in Figure 39e. The predicted spanwise velocity is a little overpredicted in the dilution jet core when compared to the experimentally measured results but overall, the results agree well with each other. When comparing the turbulence intensity contour of the experimental results shown in Figure 39c to the predicted results shown in Figure 39f, the turbulence intensity is severely underpredicted within the dilution jet and downstream of the dilution jet. In all three contours it can be seen that the jet penetration is underpredicted for the realizable k-ε simulation when compared to the experimental results. When looking at the predicted streamlines, the streamlines are well predicted upstream of the dilution jet. Within the dilution jet the streamlines follow the jet as expected and show the underpredictions of the jet penetration clearly. Downstream of the dilution jet, the predicted streamlines do not match well with the experimental streamlines.

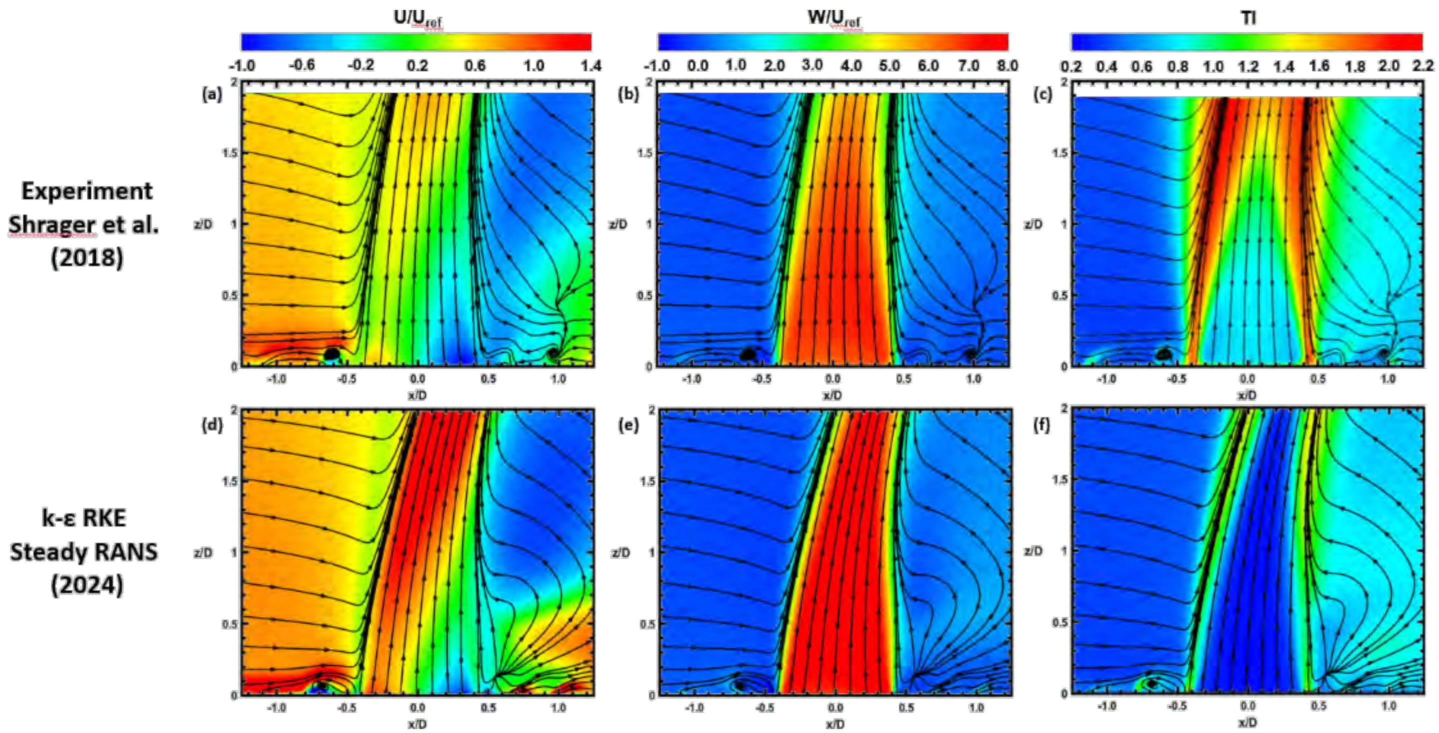

Figure 39. Experimentally measured (a) normalized axial velocity, (b) normalized spanwise velocity, and (c) turbulence intensity contours with streamlines overlaid from Shrager et al. (2018) compared to realizable k-ε turbulence model predicted (d) normalized axial velocity, (e) normalized spanwise velocity, and (f) turbulence intensity contours with streamlines overlaid for the outward facing effusion hole configuration with a dilution jet momentum flux ratio of I = 30 and a turbulence intensity of TI = 13.

The severe underprediction of the turbulence intensities and jet penetration led to further investigation into the current simulation's inlet boundary conditions. To produce the correct inlet turbulence boundary conditions, a RANS and LES simulation was completed this reporting quarter that included the turbulence bar grid used in the experiment. Both the RANS and LES bar grid simulations were run using the geometry domain shown in Figure 40 that extends the full wind tunnel height of 0.55 m and the full wind tunnel width of 1.11 m of the experimental setup. The boundary conditions include an inlet velocity set to a uniform 3.4 m/s with the bar grid located 15 bar diameters upstream of the computational domain inlet corresponding to the Shrager experiments. The domain exit boundary condition was set as a static pressure outlet with the pressure being equal to the experiment atmospheric pressure and was located at the same axial position as the exit for the computational domain. The simulation using the LES bar grid was run for four flow field times before any results were extracted to ensure the results were statistically stationary. A flow field time was defined and calculated by dividing the total domain length by the volume average axial velocity, as calculated from the RANS simulation. Once the bar grid simulation was considered statistically stationary, results were collected for an additional 9.5 flow field times. An appropriate timestep was determined after the bar grid LES solution had been initialized so that the convective Courant number was never greater than unity. After each statistically stationary timestep a table was exported containing values for the three components of velocity and static temperatures for each cell located on the blue plane, as designated in Figure 40. Once the simulation was completed, a master table that varied with time was imported into the domain and upon running RANS and LES, the turbulence decay from the grid bars to the experimental measurement plane agreed very well. This process provided the correct inlet boundary conditions to help further evaluate the poor prediction of the jet penetration and turbulence levels.

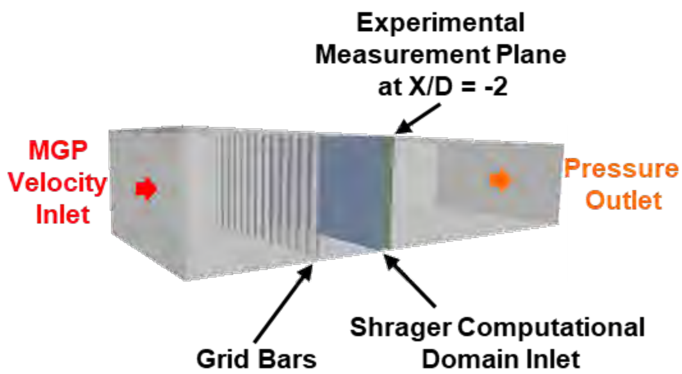

Figure 40. Bar grid domain used to extract inlet boundary conditions for the computational simulations corresponding to the Shrager experiments.

Rerunning the computational simulations of the Shrager experiments using the realizable k-ε RANS and LES models with the new inlet boundary conditions did improve the solution stability; however the jet penetration and turbulence levels were still severely underpredicted. A thorough analysis was then completed by examining the original particle image velocimetry (PIV) data from Shrager et al. (2018) to ensure the reported turbulence levels were not artificially elevated due to PIV processing settings, and that the reported momentum flux ratio was correct. The results of this recent in-depth analysis indicated the turbulence levels were not artificially elevated due to the chosen PIV processing settings. It was found that the PIV settings originally chosen were appropriate for the data, and high turbulence levels reported at the core of the jet can be attributed to the selected turbulence intensity nondimensionalization parameter. The turbulence intensity definition in the denominator used the average main gas path (freestream) velocity located at the domain inlet.
The average freestream velocity was only 3.4 m/s while the velocity fluctuations within the dilution jet flow were around the same order of magnitude. This similarity between the jet flow velocity fluctuations and freestream velocity leads to higher dilution jet turbulence intensities than if the fluctuations were nondimensionalized by the dilution jet's local mean velocity. The dilution jet's mean velocity is an order of magnitude higher than the jet velocity fluctuations. When the dilution jet turbulence levels are defined using local jet velocities, the turbulence levels compare better to what is expected. In addition, the recent in-depth analysis showed that the momentum flux ratio reported by Shrager et al. (2018) was correct. A 2.8% and 2.9% error were seen when comparing the RANS dilution and effusion jet momentum flux ratios to the experimental data, respectively.

Beginning in January of 2024, manufacturing was started on the various profile simulator hardware components. Currently, the hardware components are 90% complete through the manufacturing process, and the estimated completion of all simulator components is mid-November 2024. Before the simulator is shipped to PSU, a trial fit of all main hardware components will be performed. This trial fit will ensure the components mate with each other as intended and none of the parts have to go back out for machining rework. This trial fit process will save PSU valuable time when the simulator arrives.

Over the past year, work was performed to begin procuring other miscellaneous parts that are needed for experimentally testing the simulator, such as the 360° traverse components, flow valves, flow meters, and general instrumentation. An instrumentation plan is being developed to establish (1) a bill of materials for the instruments and sensors that need to be ordered, (2) the details related to instrumentation installation and placement, and (3) the details related to the egress of sensor tubes and wires. The instrumentation will include temperature, pressure, and flow measurement devices placed throughout the simulator device to dial in experimental operation settings that enable the simulator to produce the target profiles. In addition, these measurement instruments can help aid in CFD validation by providing accurate experimental data that can be compared back to the computational predictions.

Milestones

Milestone	Completion Date	Status
Workplan	3/5/20	Completed
COE Meeting 1	10/29 - 10/29/21	Completed
COE Meeting 2	10/26 - 10/28/22	Completed
COE Meeting 3	10/24/23	Completed
COE Meeting 4	10/29 - 10/31/24	Completed
Annual Report	12/13/24	Completed

Major Accomplishments

- Successfully demonstrated improved dirt management for combustor liners through the implementation of a triple-wall cooling design. (Task 2)
- Completed manufacturing of the combustor profile simulator. In addition, more detailed computational predictions of the flowfield to meet the needs of the START facility have been completed with higher fidelity simulations being ramped up. (Task 3)

Publications

McFerran, K., Thole, K. A., & Lynch, S. P. (2025). Dirt ingestion impacts on cooling within a double-walled combustor liner. *ASME Journal of Turbomachinery, 147*(8), 081019. https://doi.org/10.1115/1.4067464

Schaeffer, C. B., Barringer, M. D., Lynch, S. P., & Thole, K. A. (2025). Influence of dilution and effusion flows in generating variable inlet profiles for a high-pressure turbine. *ASME Journal of Turbomachinery*, 147(3), 031003. https://doi.org/10.1115/1.4066560

Schaeffer, C. B., Barringer, M. D., Lynch, S. P., & Thole, K. A. (2025). *Comparison of predicted and measured combustor-relevant flow fields* (GT2025-15782). (in progress).

Outreach Efforts

- Presented periodically to Pratt & Whitney through this joint collaboration.
- Presented the combustor simulator concept to the U.S. Department of Energy, Siemens Energy, Honeywell, and Pratt & Whitney. Industry partners are very supportive of this direction and provide guidance.

Awards

Chad Schaeffer won a third-place poster award for a poster focused on the profile simulator design and corresponding computations that he presented at the National Aeronautics and Space Administration (NASA) ImaginAviation University Poster Session.

Student Involvement

Kyle McFerran earned his Master of Science in Mechanical Engineering in August 2024. Kyle started working for Pratt & Whitney starting in September 2024. Chad Schaeffer is performing CFD simulations and assisting in the design of the combustor profile simulator. Chad successfully passed the PhD comprehensive examination in April 2024. All students participate in weekly meetings with their advisors (Berdanier/Thole/Lynch) and in regular meetings with Pratt & Whitney. They regularly present their findings to Pratt & Whitney, including to a larger Pratt & Whitney audience at the biannual Center of Excellence meetings (June and November).

Plans for Next Period

- Optimize the multi-wall combustor liner design and evaluate associated heat transfer performance benefits (Task 2).
- Begin integration for the profile simulator into the START rig and continue with higher fidelity computational simulations (Task 3).

References

Barringer, M. D., Thole, K. A., & Polanka, M. D. (2004, June 14-17). Developing a combustor simulator for investigating high pressure turbine aerodynamics and heat transfer. *Proceedings of the ASME Turbo Expo 2004: Power for Land, Sea, and Air. Volume 3: Turbo Expo 2004,* Vienna, Austria. https://doi.org/10.1115/GT2004-53613

Choi, W., & Kim, S. (2022). Effect of effusion hole arrangement on jet array impingement heat transfer. *International Journal of Heat Mass Transfer, 192*, 122900.

Fallon, B., McFerran, K., Fox, S., Thole, K.A., & Lynch, S.P. (2023, June 26-30). Comparison of dirt deposition on double-walled combustor liner geometries. *Proceedings of the ASME Turbo Expo 2023: Turbomachinery Technical Conference and Exposition. Volume 13C: Turbomachinery — Deposition, Erosion, Fouling, and Icing; Design Methods and CFD Modeling for Turbomachinery; Ducts, Noise, and Component Interactions*, Boston, Massachusetts

Gardon, R., & Akfirat, J.C. (1965). The role of turbulence in determining the heat-transfer characteristics of impinging jets. *Journal of Heat Mass Transfer, 8*(10), 1261-1272.

Gardon, R., & Akfirat, J.C. (1966). Heat transfer characteristics of impinging two-dimensional air jets. *Journal of Heat Mass Transfer, 88*(1), 101-107.

Karalus, M., Krishnamoorthy, N., Reynolds, B., & Mallouppas, G. (2019, June 17-21). An assessment of the implicit non-iterative PISO solution procedure for the prediction of combustor performance. *Proceedings of the ASME Turbo Expo 2019: Turbomachinery Technical Conference and Exposition. Volume 4B: Combustion, Fuels, and Emissions*, Phoenix, Arizona. https://doi.org/10.1115/GT2019-90950

Lundgreen, R. K. (2017, June 26-30). *Pressure and temperature effects on particle deposition in an impinging flow proceedings of the ASME Turbo Expo 2017: Turbomachinery Technical Conference and Exposition. Volume 2D: Turbomachinery*, Charlotte, North Carolina. https://doi.org/10.1115/GT2017-64649

McFerran, K., Thole, K. A., & Lynch, S. P. (2025). Dirt ingestion impacts on cooling within a double-walled combustor liner. *ASME Journal of Turbomachinery, 147*(8), 081019. https://doi.org/10.1115/1.4067464

OEM Engine Manufacturers. (2022). *Private communication with OEM engine manufacturers requesting combustor exit profiles at the vane inlet.*

Povey, T., Chana, K. S., Jones, T. V., & Hurrion, J. (2007). The effect of hot-streaks on HP vane surface and endwall heat transfer: An experimental and numerical study. *ASME Journal of Turbomachinery, 129*(1), 32–43. https://doi.org/10.1115/1.2370748

Shrager, A. C., Thole, K. A., & Mongillo, D. (2018). Effects of effusion cooling pattern near the dilution hole for a double-walled combustor liner—Part II: Flowfield measurements. *ASME Journal of Engineering for Gas Turbines and Power, 141*(1), 011023. https://doi.org/10.1115/1.4041153

Shrager, A. C., Thole, K. A., & Mongillo, D. (2019). Effects of effusion cooling pattern near the dilution hole for a double-walled combustor liner—Part 1: overall effectiveness measurements. *ASME Journal of Engineering for Gas Turbines and Power, 141*(1), 011022.

Singh, S., Reagle, C., Delimont, J., Tafti, D., Ng, W., & Ekkad, S. (2013). Sand transport in a two pass internal cooling duct with rib turbulators. *International Journal of Heat and Fluid Flow*, 46, 158-167. https://doi.org/10.1016/j.ijheatfluidflow.2014.01.006

Disclaimer

This research was funded by the U.S. Federal Aviation Administration Office of Environment and Energy through ASCENT, the FAA Center of Excellence for Alternative Jet Fuels and the Environment, Project 68 through FAA Award Number 13-C-AJFE-PSU-109 under the supervision of Joshua Glottmann. Any opinions, findings, conclusions or recommendations expressed in this material are those of the authors and do not necessarily reflect the views of the FAA.